Integrating Materials and Manufacturing Innovation (2019) 8:194–216
https://doi.org/10.1007/s40192-019-00133-8

THEMATIC SECTION: ADDITIVE MANUFACTURING BENCHMARKS 2018

LPBF Right the First Time—the Right Mix Between Modeling and Experiments

Mustafa Megahed[1] · Hans-Wilfried Mindt[1] · Jöerg Willems[1] · Paul Dionne[2] · Lars Jacquemetton[3] · James Craig[4] · Piyush Ranade[5] · Alonso Peralta[6]

Received: 18 January 2019 / Accepted: 21 March 2019 / Published online: 18 April 2019
© The Minerals, Metals & Materials Society 2019

Abstract

Laser powder bed fusion (LPBF) is an additive manufacturing process with many adjustable input parameters that directly affect manufacturability and quality of the final product. The selection of the optimal input parameters makes the process qualification and part certification a costly and time-consuming task if performed using the traditional sequential and empirical approach.

Within the scope of the DARPA open manufacturing program, a rapid qualification framework is developed that relies on parallel multi-physics modeling and experimental efforts for verification and validation of the process input parameters during process development and material characterization. Product manufacturability is tested a priori via modeling and in-process monitoring is deployed to ensure input parameters are rapidly screened, and an optimal process window is selected. Process consistency and repeatability is further ensured through process characterization, process qualification, and via quantitative analysis of digital In-Process Quality Metrics™ (IPQM®s).

This paper discusses the rapid qualification methodology, model validation, and the application of the framework towards manufacturing of a challenging part defined by AFRL. The combination of numerical predictions, experimental refinement, and in-process monitoring delivered the first print right at first trial. Distortions are within predictions, geometric accuracy is within expectations, and quantitative metallurgical analysis shows dense as-built material with properties expected to fulfill performance requirements. In-process monitoring results provide a quantitative, digital Quality Signature™ or Digital Quality Record™ of process consistency and product quality.

Keywords Metal additive manufacturing · Laser powder bed fusion · Process modeling · Validation · Powder scale · Residual stress · Distortion · Simulation · Experimental validation · Certification · In-process monitoring · Process development · Process qualification · ICME · Uncertainty quantification

✉ Mustafa Megahed
Mustafa.Megahed@esi-group.com

Hans-Wilfried Mindt
Hans.Mindt@esi-group.com

Jöerg Willems
Joerg.Willems@esi-group.com

Paul Dionne
Paul.Dionne@esi-group.com

Lars Jacquemetton
lars@sigmalabsinc.com

James Craig
jcraig@stratonics.com

Piyush Ranade
piyush.Ranade@honeywell.com

Alonso Peralta
Alonso.Peralta@Honeywell.com

[1] ESI Software Germany GmbH, Kruppstr. 90, 45145 Essen, Germany

[2] ESI US R&D, 620 Discovery Drive, Suite 120, Huntsville, AL 35806, USA

[3] Sigma Labs Inc., 3900 Paseo del Sol, Santa Fe, NM 87507, USA

[4] Stratonics Inc., 25002 Castlewood, Lake Forest, CA 92630, USA

[5] Honeywell Aerospace, 12001 Highway 55, Plymouth, MN 55441, USA

[6] Honeywell Aerospace, 111 S. 34th Street, M/S 503-428, Phoenix, AZ 85034, USA

Introduction

Powder bed fusion (PBF) additive manufacturing offers unmatched design flexibility. The advantages are however hampered by the lack of design guidelines, lack of process repeatability, and the large number of possible defects that might affect workpiece performance [1, 2]. The cost associated with qualification of PBF processes and products is therefore high [3]. This paper utilizes integrated computational material engineering (ICME) supported rapid qualification platform demonstrating how combining modeling and experimental studies can be effectively used to reduce PBF process costs and risks [4].

Optimizing the process parameters relies on the use of micro models resolving the interaction between the heat source (laser in this study) and the feed stock. Analytical solutions can be used to quickly identify a process window that will require further refinement either using more detailed models or experimental studies. Kamath et al. applied the Eagar and Tsai equation to determine melt pool dimensions and process window optimization of 316L stainless steel [5]. Tang et al. used the Rosenthal equation to avoid lack of fusion defects [6]. The model used in this study is based on non-dimensional constants that characterize the conduction as well as the keyhole modes [7, 8]. High-fidelity models capturing defects originating from the process are based on computational fluid dynamics (CFD). Lattice Boltzmann-based tools are generally used for two-dimensional analysis [9–12]. Three-dimensional finite volume-based solvers resolve both conduction and keyhole regimes [13–15]. This study relies on a 3-D finite volume formulation that resolves all three thermodynamic states (solid, liquid, and vapor/gas) enabling high-fidelity resolution of pore behavior during material consolidation [16, 17]. The model is coupled to discrete element models that resolve the powder spreading (raking/recoating) process allowing for a realistic representation of the powder bed and the spreading process [18]. Macroscopic modeling of the final workpiece shape is usually performed using inherent plastic strain methods [19–24]. The model presented here relies on a novel formulation that allows improved prediction of the residual stresses while retaining the speed and accuracy of distortion predictions [8, 25, 26].

The focus of this study is the application of ICME tools previously validated [16, 18, 25, 27] in a rapid qualification platform. Some of the results have been published before; they are nevertheless included in the paper to provide the complete picture of how the ICME tools were used to qualify process parameters. In the following two sections, the rapid qualification framework and the challenge workpiece are introduced. Through sections "Identification and Optimization of Process Parameters" to "Distortion and Residual Stresses," they discuss the determination of optimal process parameters, calibration of online monitors, uncertainty quantification, and predicted residual stresses and distortions, respectively. "First Build Assessment" analyzes different quality aspects of the first build.

Rapid Qualification Framework

The probabilistic qualification/certification framework is depicted in Fig. 1, the developments under this program are enclosed in the gray box/dotted line. The peripheral items are parts of an overall certification process framework that were not addressed in this project. The dark blue headings are the areas of materials development that constitute the ICME platform. The light blue boxes depict modules that are used to analyze certain process aspects. In the green boxes, we summarize the outputs of each of those modules. The output is the knowledge developed during the program. As one moves to the right on the schematic, knowledge developed on the left gets integrated upwards such that the performance of the component is evaluated. If the performance quality criteria are predicted to be achieved, the component is built and tested. If the experimental results do not fulfill the requirements, the component needs to be re-designed or the material or process needs to be reevaluated. The ICME process is started again, where experimental data is used to improve the models' predictions.

Since the material is "created" at the same time the part is created, any new processing conditions necessitates a new creation of a full material database since the microstructure of the material may be entirely different. Such may render the application of the AM process uneconomical.

Models in dotted boxes were also used throughout the project. The uncertainties of obtained results were however not assessed.

The Rocket Nozzle

A test article was developed by Aerojet Rocketdyne under a government program sponsored by the Air Force Research Lab (AFRL) to have features representative of aerospace applications to be manufactured using laser powder bed fusion. This article was used to verify the capabilities of the ICME platform developed under the DARPA open manufacturing program for improving the manufacturability of the additive manufacturing process. As shown in Fig. 2, the specimen design incorporated multiple features of interest that are likely to be encountered in aerospace applications. Several components were built to determine the capability as well as the repeatability of the process.

Identification and Optimization of Process Parameters

The rocket nozzle is built using 718Plus [28]. The powder size distribution is shown in Fig. 3. Particles below 10 μm in diameter are filtered out to ensure powder spreadability. The chemical composition of the powder was confirmed to be within the specifications.

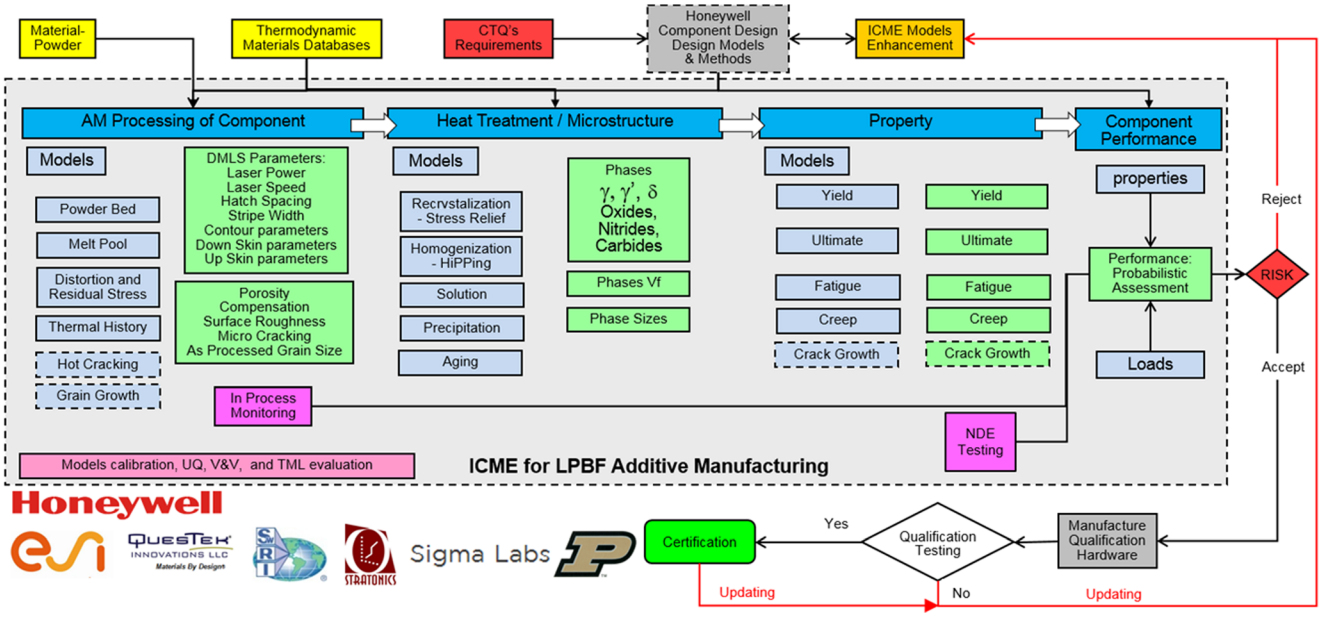

Fig. 1 Probabilistic certification framework

Quick Numerical Identification

An optimization scheme based on non-dimensional variables was used to identify optimal process parameters [8]. Four design (optimizable) parameters are varied: laser power, scan speed, hatch spacing, and layer thickness to achieve maximum material density and maximum deposition rate. The optimization was constrained by machine capabilities; for example, the

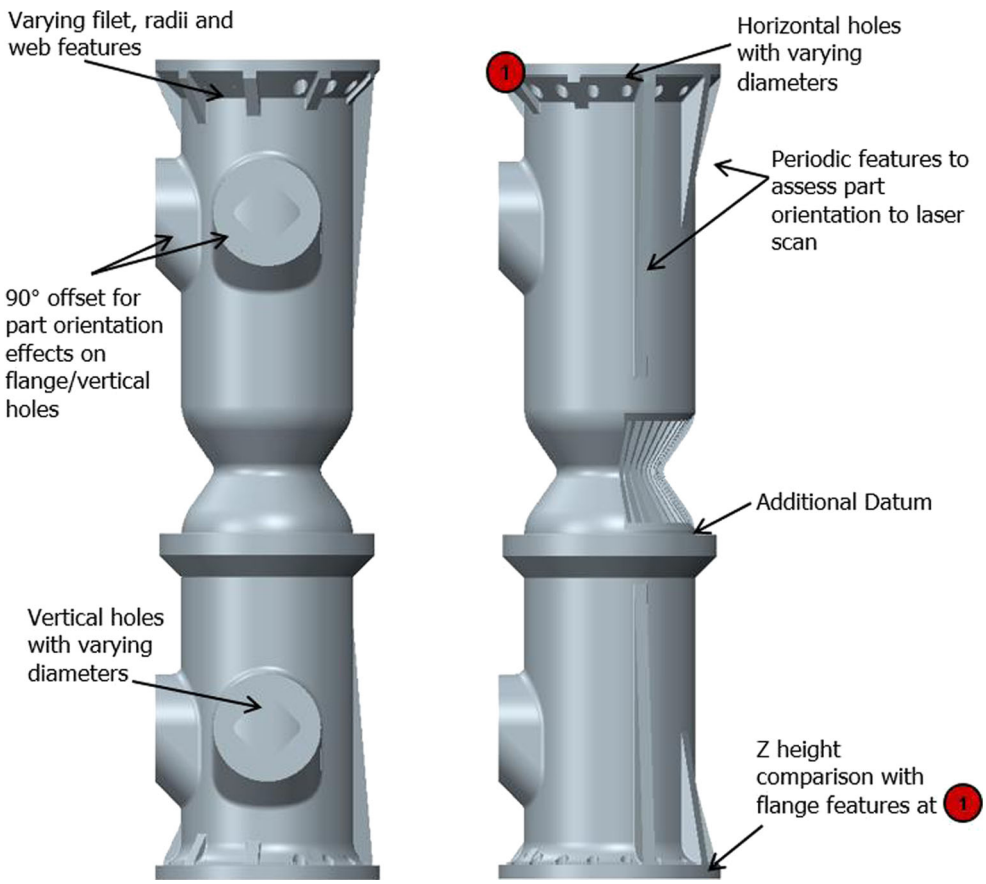

Fig. 2 Rocket nozzle

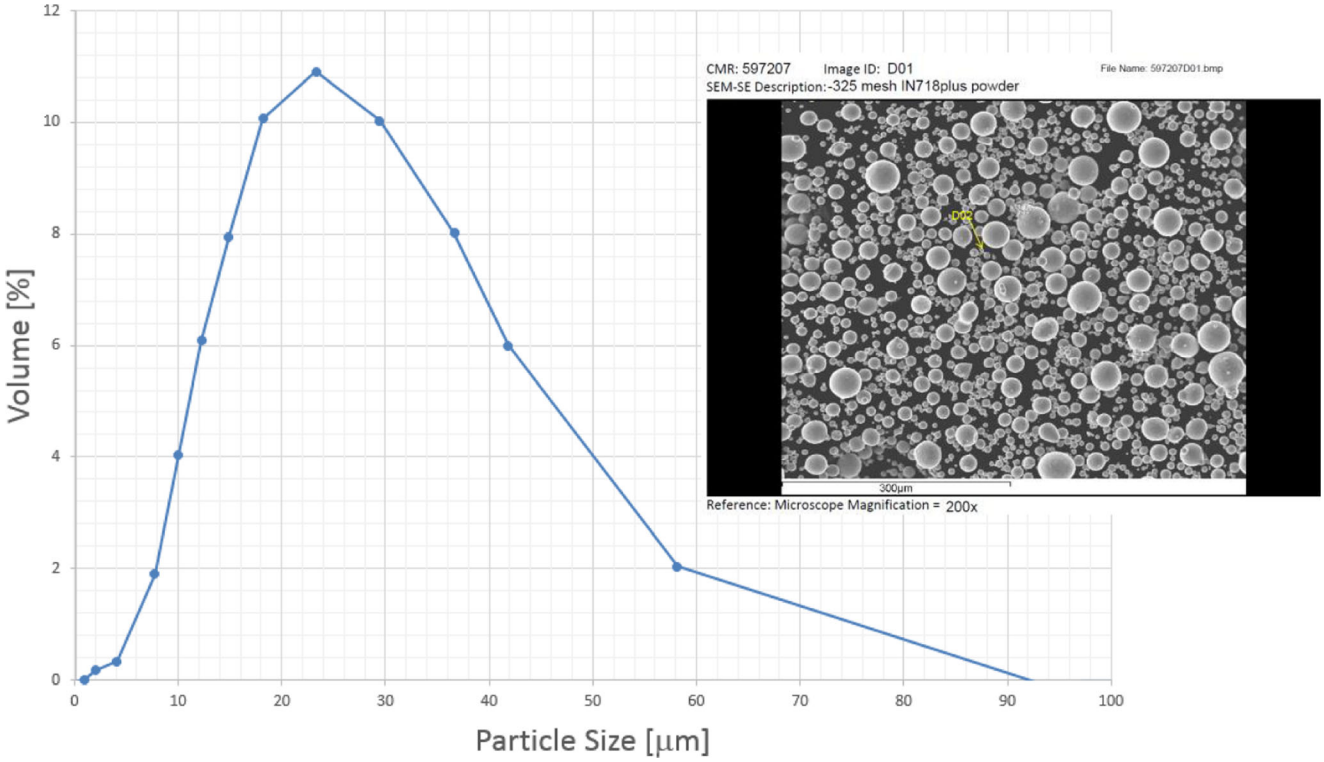

Fig. 3 718Plus powder morphology and particle size distribution

maximum power delivered by the laser is 370 W. The radar diagram shown in Fig. 4 shows the pareto front of the multi-objective optimization. The pareto front includes only those combinations that fulfill max. density, max. build rate, or the weighted sum of both cost functions. Each number on the perimeter of the radar plot represents a set of parameters that can be used. It can be readily seen that the density and the build rate are inversely proportional to one another, indicating that the optimum point will be a compromise between both optimization goals. A few points beyond the max. recommended build rate are also included to show the effect on the material quality (red triangle). In that region, the build rate is so high, that high porosity levels are visible in the micro-graphs—also included in the plot. Excluding those points in the red triangle, all the other process combinations are valid combinations delivering good material quality (as seen by the corresponding micro-graphs) and relatively high build rates. Once a point is chosen, the process parameters can be extracted and confirmed in more detailed numerical models or in experimental series confirming the choice. A point in the fourth quadrant, close to the red triangle is chosen, that will have a relatively high build rate. The corresponding build parameters are summarized in Table 1.

High Fidelity Refinement of Process Parameters

The chosen process parameters are further investigated in detail both experimentally and numerically. Multiple pillars covering the complete build plate forming an asterisk like distribution are printed (Fig. 5). The pillars' height is subdivided into eight segments. Seven of the segments are built using different sets of parameters. The last segment at the top of the pillar is built using the parameters of the first segment (closest to the build plate). By comparing the signals of segments 1 and 8, we can ensure that the chamber conditions have not changed throughout the build time. The previously identified optimum combination is used for segment 6, which leads to the lowest measured porosity 0.06%. Segments 1, 3, 4, and 7 have porosities between 0.1 and 0.3%. Segments 2 and 5 have the highest porosities, 1.1 and 12% respectively. Corresponding example micro-graphs for each of the segments are also shown in Fig. 5.

Melt pool models [16, 17] are pursued to numerically investigate material consolidation and the origin of the porosities measured. Two hatches were modeled for each of the pillar segments, as shown in Fig. 6. Near the laser spot peak temperatures around 3200 K are predicted indicating that material evaporation takes place. Once the laser passes a certain point, the molten material cools down quickly, and solidification starts. Figure 7 shows the average Archimedes porosity for each of the segments as a function of the global energy density. Side views of the modeled melt pools are also provided. The laser size and position are shown by the violet beam. The laser is moving from left to right. Segments 1, 2, 4, 5, and 6 show conduction mode melting. Case 4 is in the transition region between conduction and keyhole modes. Case 7 shows

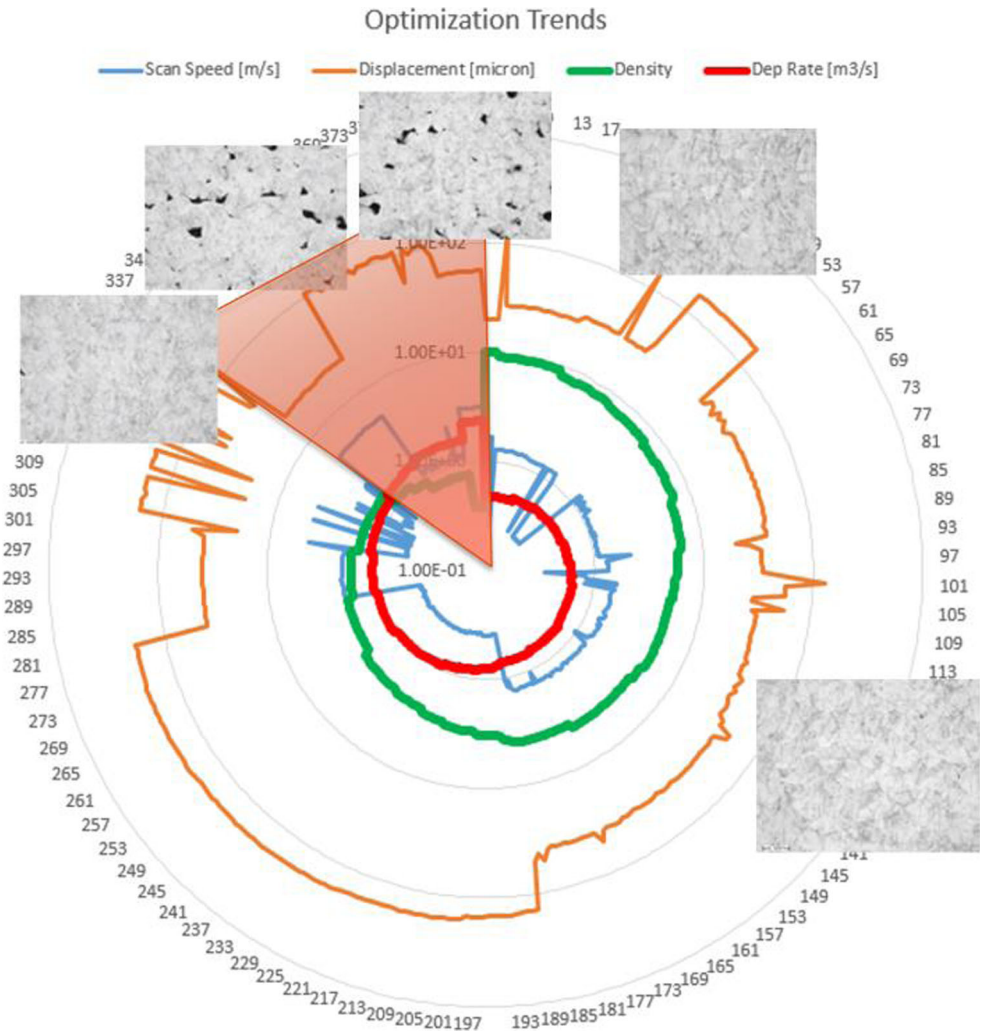

Fig. 4 Radar representation of prescan results. Process parameters are chosen to maximize material density and build rate [8]

a deep melt pool typical for keyholing. Figure 8 shows the inside of segments 2 and 7 melt pools showing several kinds of porosities. Segment 2 shows lack of fusion defects leading to non-spherical porosities. The bubbles contain shield gas that is originally between the powder particles. It is entrapped once the powder (partially) melts. In the case of keyholing (segment 7), entrapped bubbles are mostly spherical and contain a mixture of vapor and shield gas. In both cases, solidification time is much shorter than the time required by the bubbles to escape the melt pool via buoyancy. The bubble volume in the consolidated material is calculated to determine the expected material porosity.

Table 1 Preliminary combination of process parameters

	Chosen optimum
Power (W)	370
Scan speed (m/s)	1.62
Hatch spacing (μm)	90
Layer thickness (μm)	30

Figure 9 compares numerical porosity predictions with Archimedes measurements. The numerical results are validated to be accurate for the studied process parameters ranging from conduction to keyhole mode welding. The porosity of segment 6 is also confirmed to be lowest of all the process parameters considered. Segment 6 simulations and experimental validation, however, showed significant balling that lead to re-coater arm interactions (reported in [27]). The process parameters are therefore adapted by reducing the power to 300 W. All other process parameters remain unchanged.

Further melt pool information including its width, depth, and length as well as multiple characteristic temperatures such as the average melt pool temperature, average, and peak melt pool surface temperatures are also gathered from the simulations and will be used in combination with online monitors.

Multilayer Analysis

The analysis of multiple hatches enabled a good characterization of expected porosity levels. The spatial distribution of the

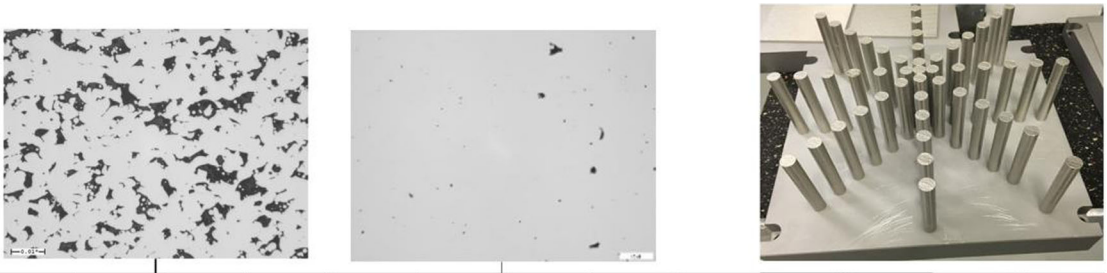

Segment	#1	#2	#3	#4	#5	#6	#7
P [W]	300	370	370	370	370	370	370
v [m/s]	1.25	3.78	0.88	1.32	2.2	1.65	0.5
H [mm]	120	140	140	140	140	90	100
GED [J/mm^2]	2	0.7	3	2	1.2	2.5	7.4
Por. [%]	0.11	12.68	0.1	0.27	1.18	0.06	0.1

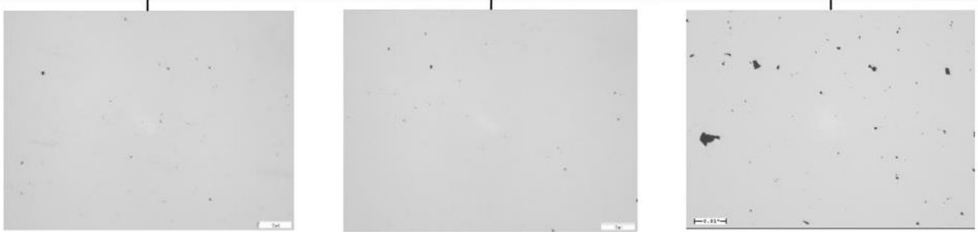

Fig. 5 Asterisk build, process parameters, and example micro-graphs

porosities and how they are affected by the deposition strategy is however not captured in those studies. Also, side surface roughness and the risk of surface porosities cannot be modeled unless several layers are analyzed. Multilayer simulations are thus pursued to analyze the spatial distribution of defects and to investigate the influence of hatch orientation on defects. Sequential powder spreading and melting is simulated to show the deposition of several layers (ten in this study). Figure 10 shows the side view of three tracks depicting the processing of a layer, which is being recoated in preparation for melting of a new powder layer.

Table 2 shows a time sequence for some of the steps modeled. The powder particles spread around the build remain loose or melt partially to contribute to the side roughness of the deposited material. Non-uniform powder distribution, different powder particle sizes and surface tension instabilities lead to a wavy surface upon which the powder spreads non-uniformly. After powder spreading of layer n, the powder is seen to fill the valleys resulting from the previously processed layer. The gray surface showing through the new powder layer is not coated. During melting of the fresh powder (layer *n*), the laser scan direction is rotated. Regions with no or very little

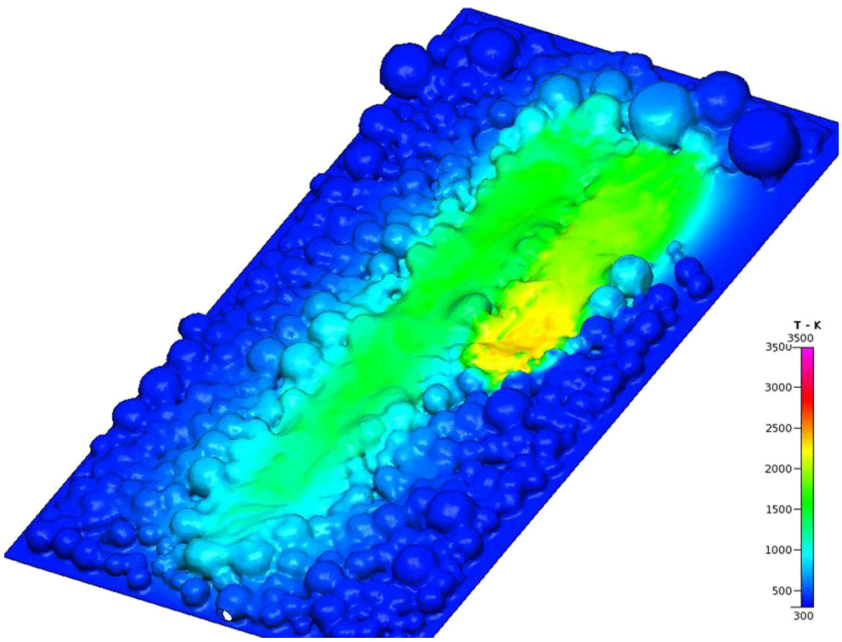

Fig. 6 Top view of two hatches colored by temperature

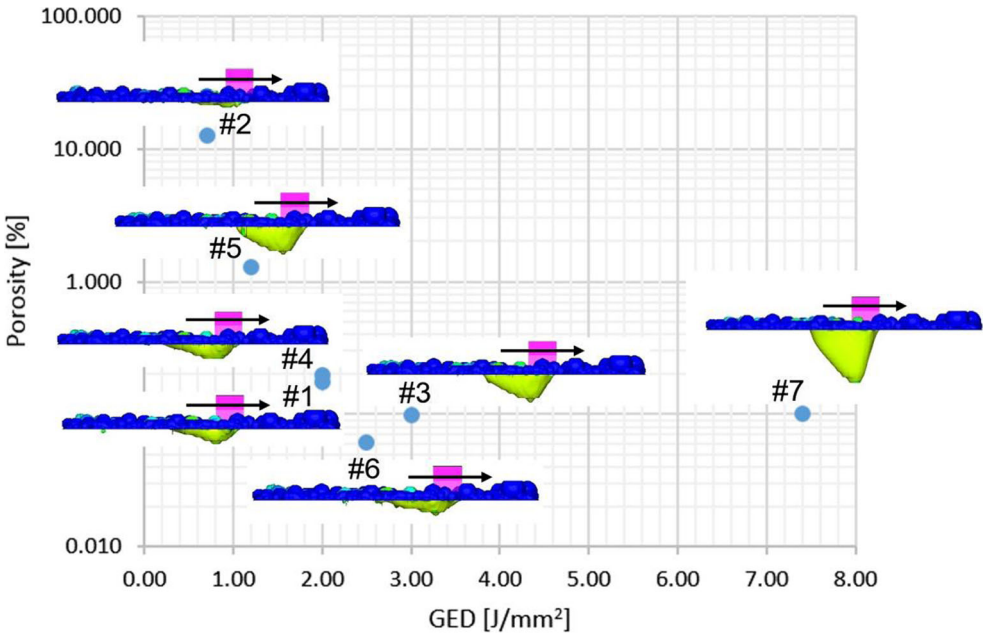

Fig. 7 Side view of melt pools numerically modeled for each of the asterisk segments. The laser moves from left to right

amounts of powder are remolten by the laser and remain at a relatively lower height after solidification in comparison to areas where larger amounts of powder are spread. During the next spreading cycle, those regions exhibit a large gap between the solidified surface and the coater arm that large amounts of powder are deposited compared to the relatively higher regions. The powder layer $n + 1$ exhibits a different distribution accordingly. The system is thus a self-correcting system trying to retain a flat surface with variations in height proportional to the gap between build and coater arm.

Figure 11 shows an example of the resulting surface roughness after solidification. Powder particles around the processed area are highest. The processed layer roughness correlates with the previous layer's topology and the powder deposition achieved. Areas that were high cannot accommodate fresh powder deposition and result in a depression of the new layer. The maximum difference in height is approximately 55 μm.

The resulting porosity in the processed volume is analyzed by translating a slice through the domain and gathering porosity values for each section. Figure 12 shows an example slice where the pores are indicated by blue. The computational cells are $5 \times 5 \times 5$ μm^3 in size. Pores that are smaller than 5 μm in diameter are assumed to not affect the part performance and will therefore not be captured by this simulation. The volumetric density is found to be 99.48% with a standard deviation of 0.4%.

Online Monitoring

Multiple online monitors are installed in the powder bed fusion system to monitor the melt pool behavior as well as the thermal emissions during the build. A 2D high-resolution high-speed camera is used that captures two wavelengths. Thermaviz® software, Stratonics Inc., is used to analyze the images to obtain the surface temperature distribution and melt pool dimensions. A calibrated spectrometer gathers all emissions from the build to provide melt pool average surface

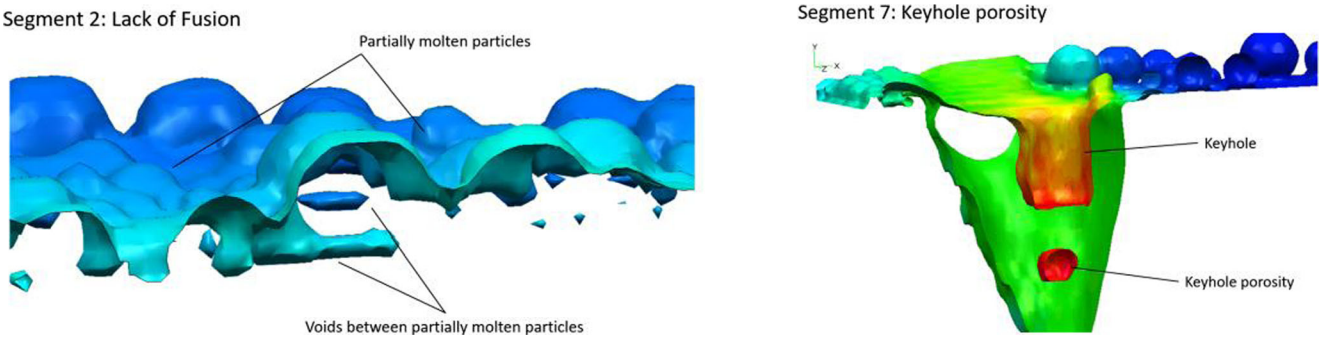

Fig. 8 Melt pool with front half of the boundary clipped away to show bubbles entrapped. Left: example of lack of fusion (segment 2). Right: example of keyhole porosity (segment 7)

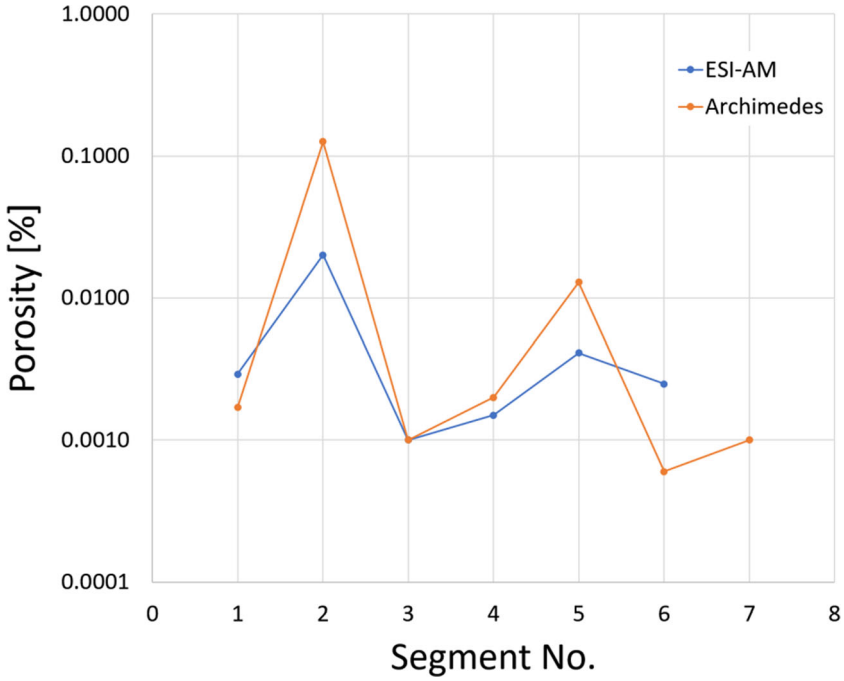

Fig. 9 Comparison of numerically predicted porosity with Archimedes measurements of asterisk build

temperature. Data collected from this system has been used to calibrate and validate the melt pool analysis.

Process consistency and repeatability is further ensured using a pyrometer with a field of view 1 mm in diameter focused on a reference feature in the build and a photodiode. When in-process data collected from the photodiode is mined for features and fused to derive in-process quality metrics™ ("IPQM®s"), a complete understanding of part quality and of process control can be obtained. Sigma labs also installed a position sensor in-line with the command signal coming from the EOS computer to the scanhead to capture and record *x-y* position information of the laser. Such data is used to correlate laser position information with IPQM®" data generated with Sigma's PrintRite3D software. Therefore, allowing the capability to monitor the build throughout the full bed.

Temperature Predictions and Measurements

The high-resolution high-speed camera is installed in such a way that it looks directly downwards on the build plate. In this position, the field of view is not skewed but it is hampered by the vapor plume generated during the process. An alternative oblique installation was also utilized to avoid having to capture information through the vapor plume. The disadvantage in this case is that the field of view is affected by the angle at

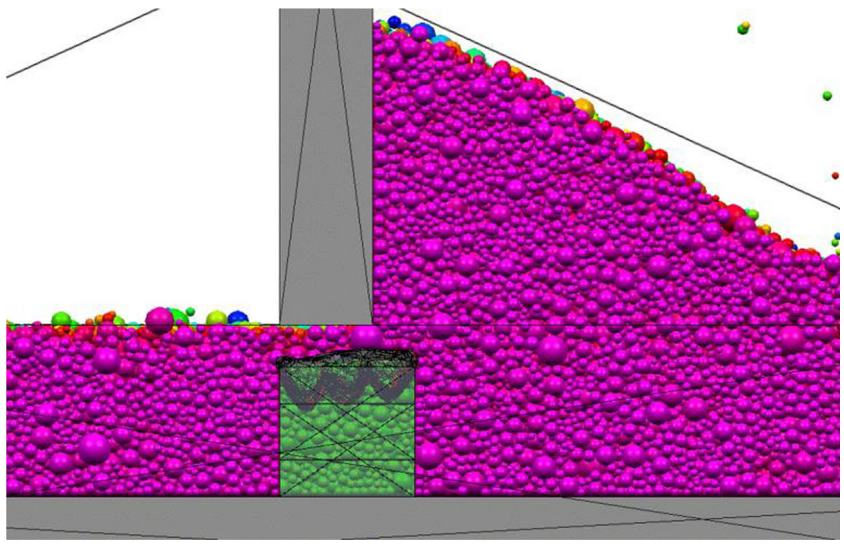

Fig. 10 Recoating of processed area (shown in transparent mode)

Table 2 Time sequence of several powder spreading and melting steps to create a multilayer deposit

Layer n	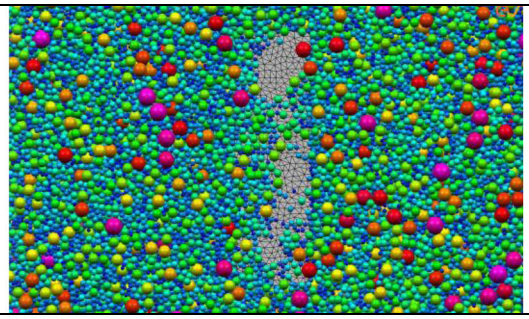	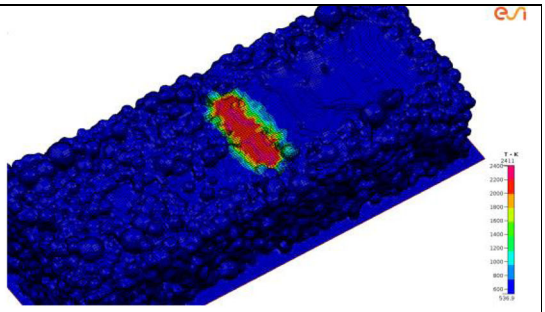
Layer n+1	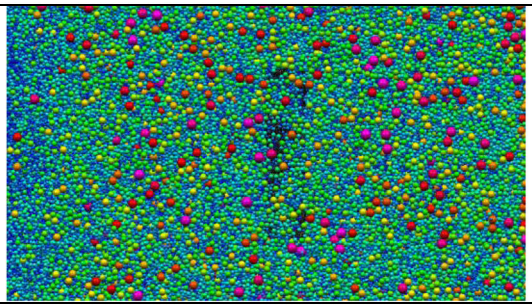	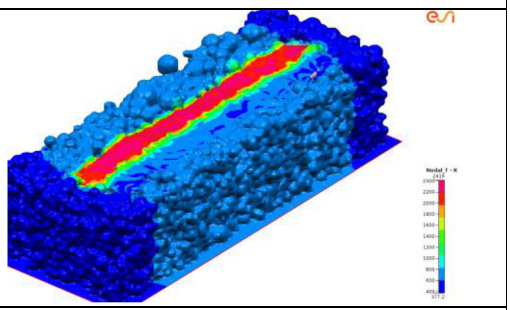
Layer n+2	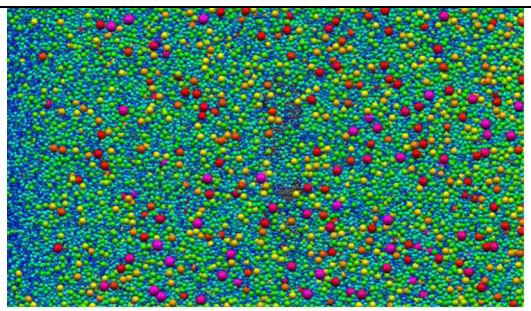	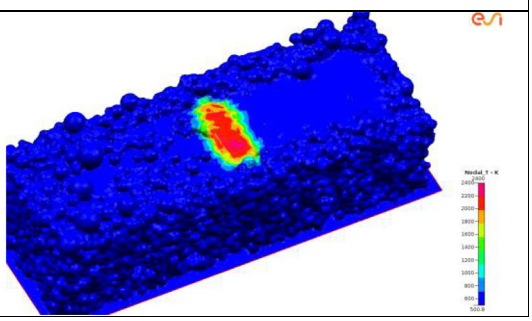

which the camera is installed. ThermaViz® is used to calculate the average temperatures monitored for several layers.

A spectrometer is also used to measure the powder bed surface temperature using emissions gathered at a

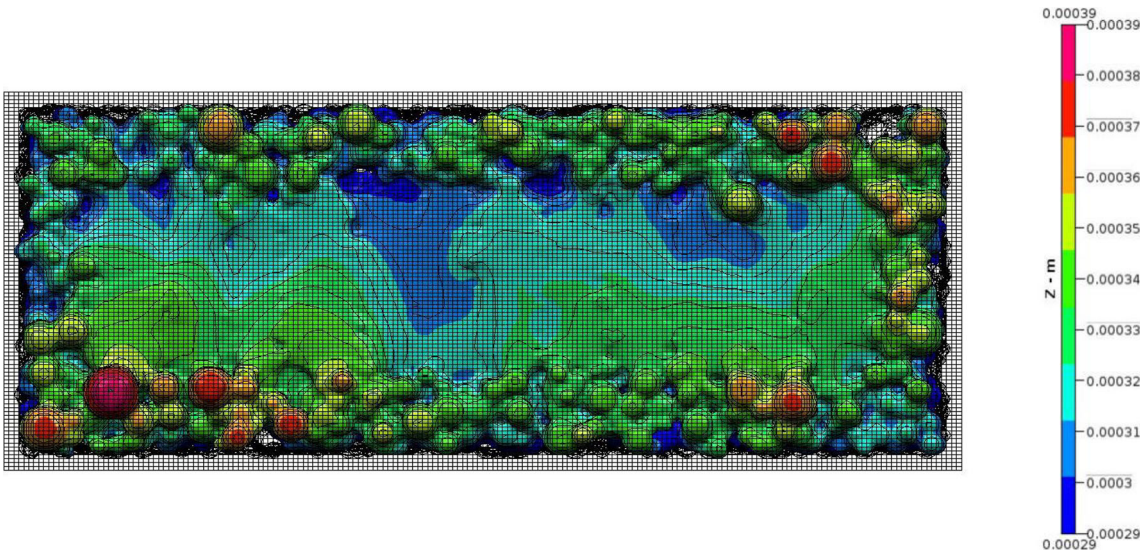

Fig. 11 Exemplary top view of processed surface. Colors show height

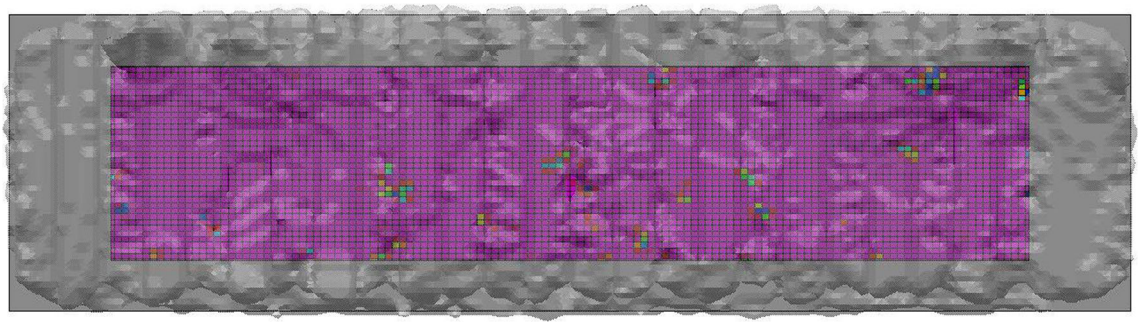

Fig. 12 Slice through numerical build, cold colors indicate pores that are at least 5 μm in diameter

wavelength of 700 nm. To compare predicted temperatures with spectrometer measurements the spectral emissions expected from the modeled powder bed is calculated using Planck's law. The emission at 700 nm is calculated for every computational cell on the powder bed surface using the predicted surface temperature. The area weighted sum of surface emissions is then used to obtain a "numerical spectrometer temperature"—again—using Planck's law.

All four temperature values are compared for laser power of 300 W at different scan speeds in Fig. 13.

The vertical and oblique camera positions lead to a maximum difference of 150 K in the temperature measurements. The spectrometer measures the highest values. The measurements deviate by maximum 200 K from one another. The numerical predictions are within the bounds of all measurements except for the highest scan speed studied. Given temperature values in the order of 2500 K, the maximum error of numerical predictions is estimated to be lower than 8%.

Calibration In-process Quality Assessment

Figure 14 shows a typical output of the in-line quality assessment tool gathering the pyrometer and photodiode signals. If the signal deviates from the reference signals, the point is flagged in red. In the asterisk experiment, we have seen that only segments 2 and 5 lead to unacceptable porosities. Yet, the system is also flagging sections 3 and 4 to have problems.

In order to investigate this discrepancy, the thermal history predicted by the melt pool models for sections 2, 3, and 5 are compared. Three monitor points are chosen as described in [17] (Fig. 15). The upper most monitor point is closest to the melt pool surface. The lowest point is positioned to be at the melt pool base, near the solid surface. A third point between the highest and lowest point monitors the melt pool temperature. Previous studies indicated that good material consolidation with a minimum number of pores show almost identical thermal histories for all three monitor points. This is attributed to

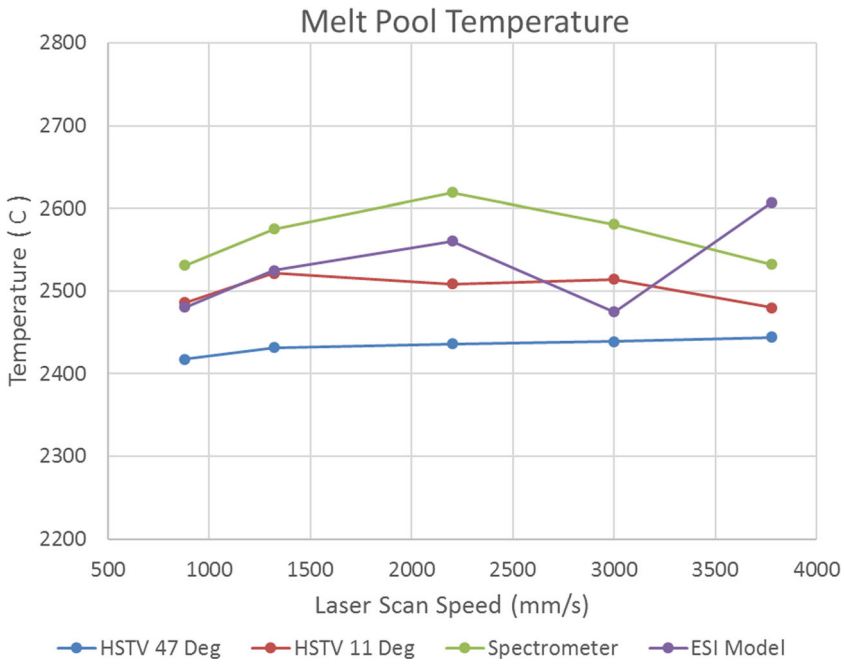

Fig. 13 Comparison of melt pool temperature measured using vertical camera, oblique campera, spectrometer, and melting model

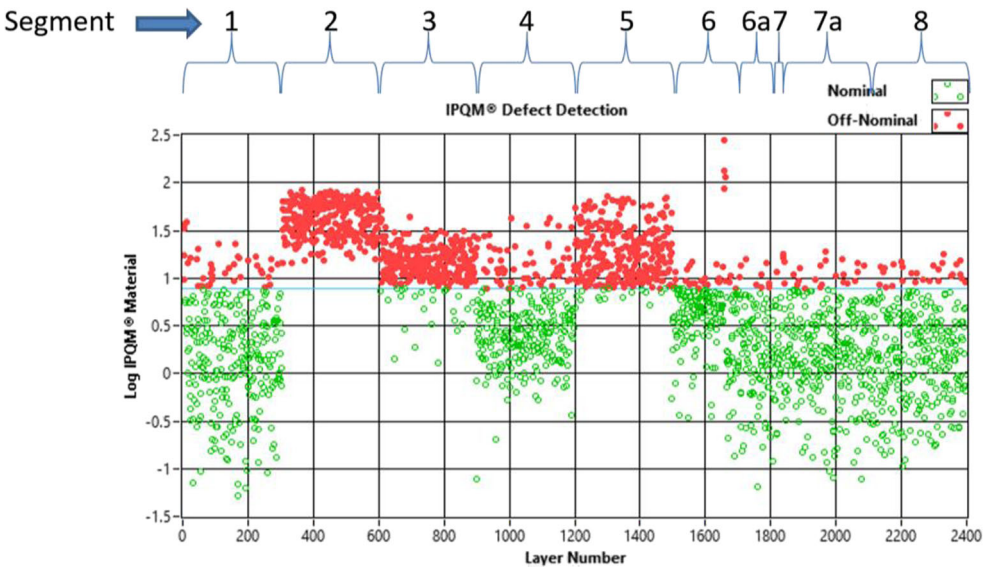

Fig. 14 In-process quality assessment for the seven asterisk segments. Red indicates a deviation from the specified nominal behavior

Marangoni convection, which homogenizes the melt pool temperature. If a lot of pores exist in and around the melt pool, Marangoni convection and conduction are both hampered by the gas pores. The temperature at the melt pool base follows that of the melt pool and the surface with a significant time delay.

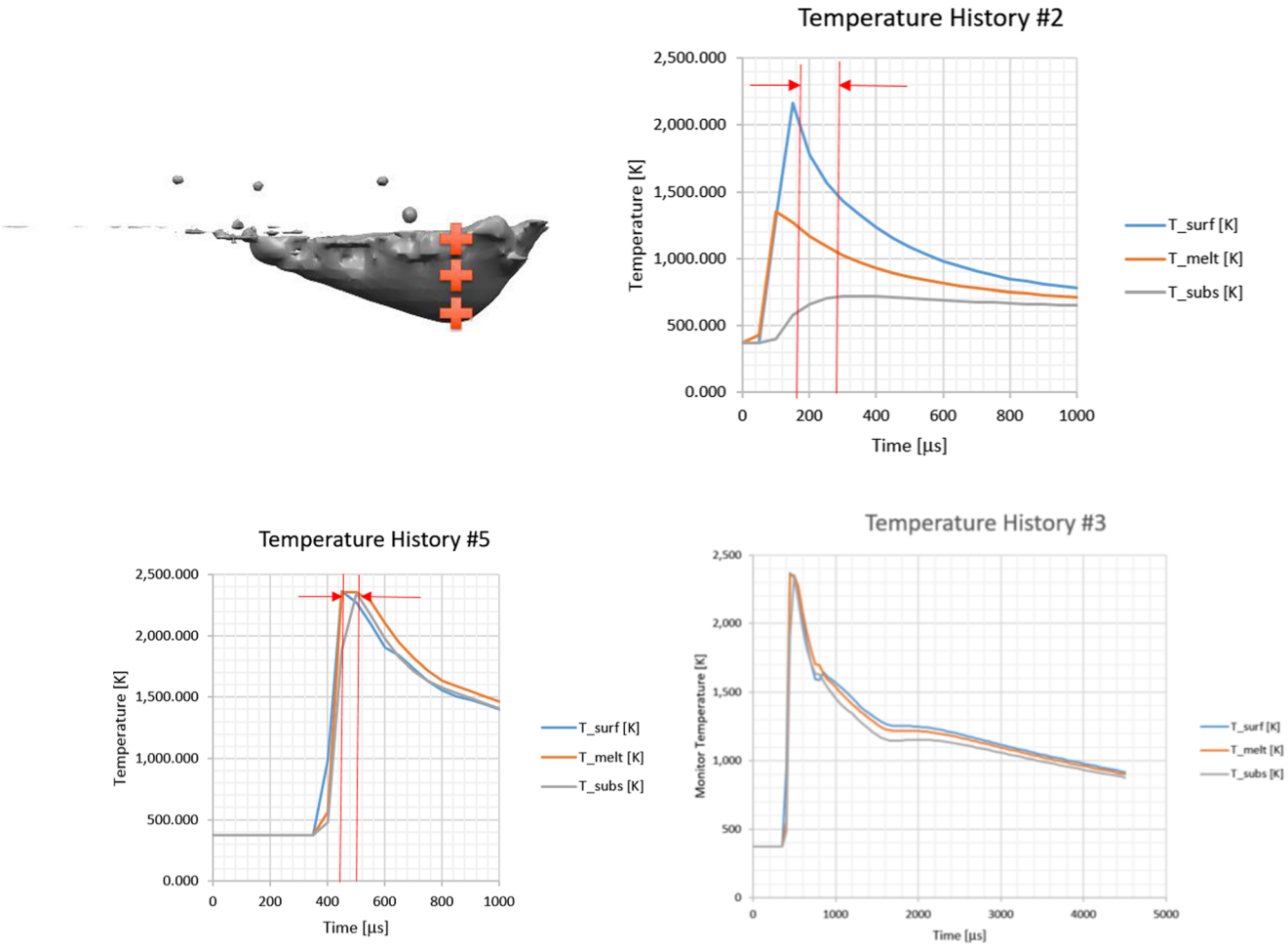

Fig. 15 Thermal history for segments 2, 3, and 5. The temperature data is shown for three points in the melt pool: at the surface, at mod-depth, and at the lower boundary of the melt pool (see schematic representation of monitor points)

Considering the thermal histories for segments 2 (Fig. 15) readily shows that the melt pool bottom thermal history lags behind that of the surface temperature confirming the bad quality of the consolidated material. Segment 3 shows almost identical thermal histories for all three monitoring points confirming perfect heat exchange within the melt pool and low levels of porosity. The behavior of segment 5 is between these extremes with the bottom thermal history showing a minimal time delay compared with the surface temperature. Simulations thus indicate that segment 2 has significant consolidation problems, segment 5 is not as bad, and segment 3 is actually a good build.

In order for the in-line quality assessment to show the same results, the threshold defining "good" and "bad" conditions is adapted as shown in Fig. 16. With the adapted threshold, the online monitoring system will indicate the relative build quality accordingly. If segments 1, 3, and 4 are to be considered less favorable in tighter tolerance scenario, the threshold can be returned to the previous setting.

Uncertainty Quantification and Process Map

First, we study the influence of powder bed variation. Figure 17 shows a powder bed as predicted by the spreading model [18]. The powder size distribution is digitized and discretized into ten bins. The process parameters identified in prescan and melting modules and in particular the table displacement is used. It can be readily seen that the powder does not spread uniformly on previously processed surfaces. To study the variation in powder distribution and packing density, five domains with different characteristics are chosen to study the influence of the powder bed distribution on material consolidation and porosity.

The domains are chosen interactively to include regions with no particles, large particles, small particles, and a mix of small and large particles. Figure 17 shows the domains chosen for the analysis. Results gathered from melt pool simulations include average consolidated material porosity, average melt pool temperature, and melt pool dimensions. The results are provided in Figs. 18, 19, and 20. The porosity of the spread powder bed varies between 30 and 40% (Fig. 18). After laser processing, the material consolidates to a porosity of approximately 10%. The porosity of the powder bed is calculated based on the number of particles spread and the volume they occupy. The porosity of the consolidated material is analyzed along the studied melt beads. An average porosity is calculated for the consolidated material with the corresponding standard deviation. The trend in porosity variation from one domain to the other can still be seen in the porosity of the consolidated material. This indicates that the quality of powder spreading does affect final material quality but the standard deviation along the processed tracks are large enough to consider the final porosity to be very similar. The differences between average melt pool temperatures are negligible and the melt pool dimensions are almost identical. This result was to be expected because they mainly depend on the laser power, scan speed, and hatch spacing, and not directly on the powder distribution. It is thus concluded that powder bed

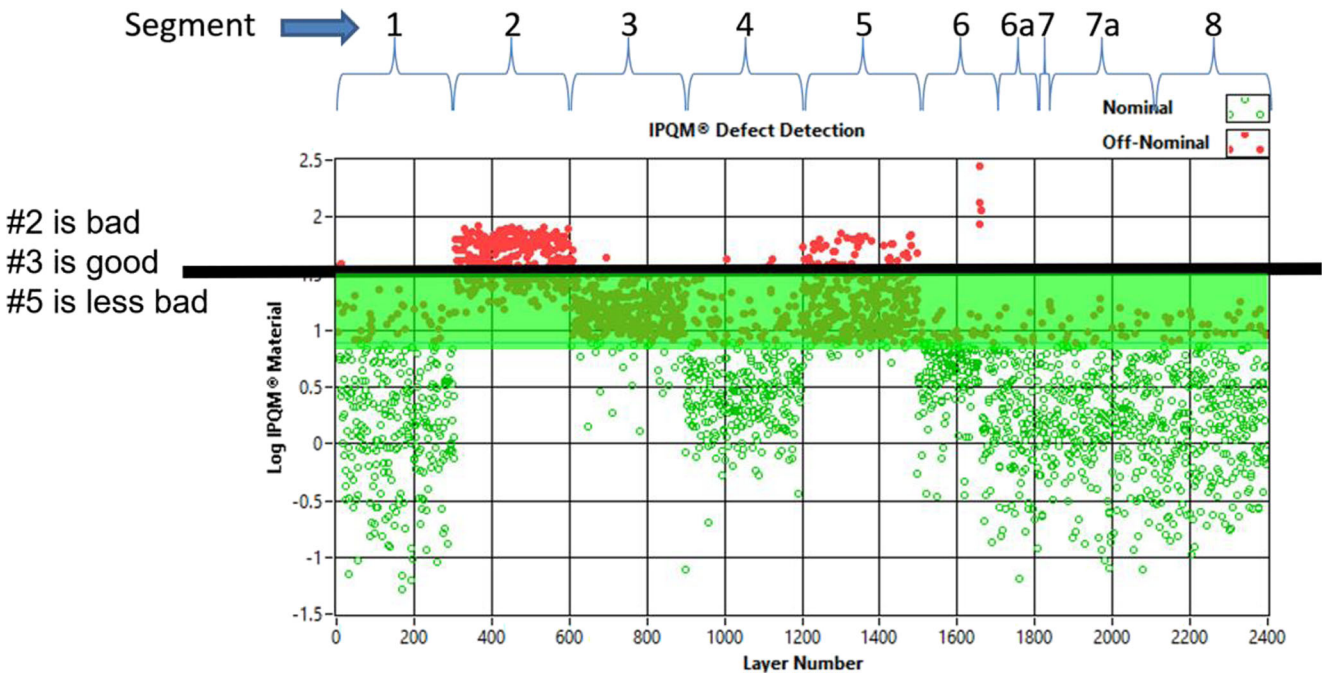

Fig. 16 In-process quality assessment with adapted threshold for the seven asterisk segments. Red indicates a deviation from the specified nominal behavior

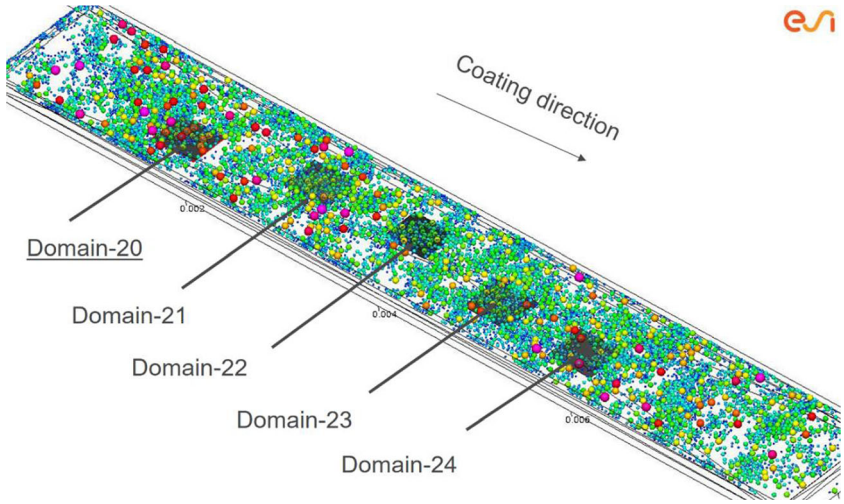

Fig. 17 Non-uniformity of powder bed on previously processed material

variations might affect the final porosity but within 10% of the nominal packing density the final material porosity is not affected by the powder bed packing density.

The uncertainty in processing parameters is studied next. Table 3 summarizes the nominal process parameters values as well as the upper and lower bounds of variation. Table displacement and hatch spacing are assumed to be reliably followed by the printer. When using Latin hyper cube sampling, a numerical DOE with 150 cases is created. When using proper generalized decomposition of the parameter space with level 2 accuracy, 136 cases are defined [29, 30].

The numerical DOE porosity predictions are plotted against the global energy density in Fig. 21. The porosity of each of the studied conditions is an average along the simulated melt bead. The corresponding average deviations are shown as error bars. GED is defined as the ratio between power and the product of scan speed and hatch spacing. A minimum porosity is expected at a GED of 2.1. Conduction mode melting (GED < 2) show tightly clustered results with relatively small error bars. The results scatter increases as GED increases. For keyhole mode (GED > 2.5) the results show large scatter and larger error bars indicating that the process is less stable.

It is important to note that GED is not a complete representative of process parameter combinations. Different process combinations can be used to achieve the same GED but different melt pools will result from these combinations [31].

A process map is created to assess the size of the process window and the uncertainty of the predictions (Fig. 22). In regions of high power and low scan speeds the keyholing

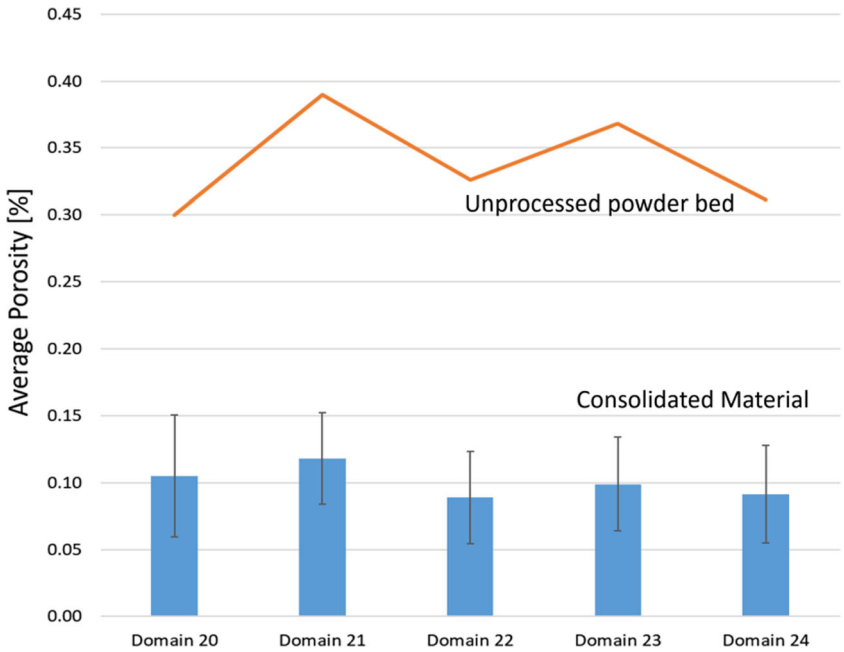

Fig. 18 Porosity of powder bed and of consolidated material from domains 1 to 5

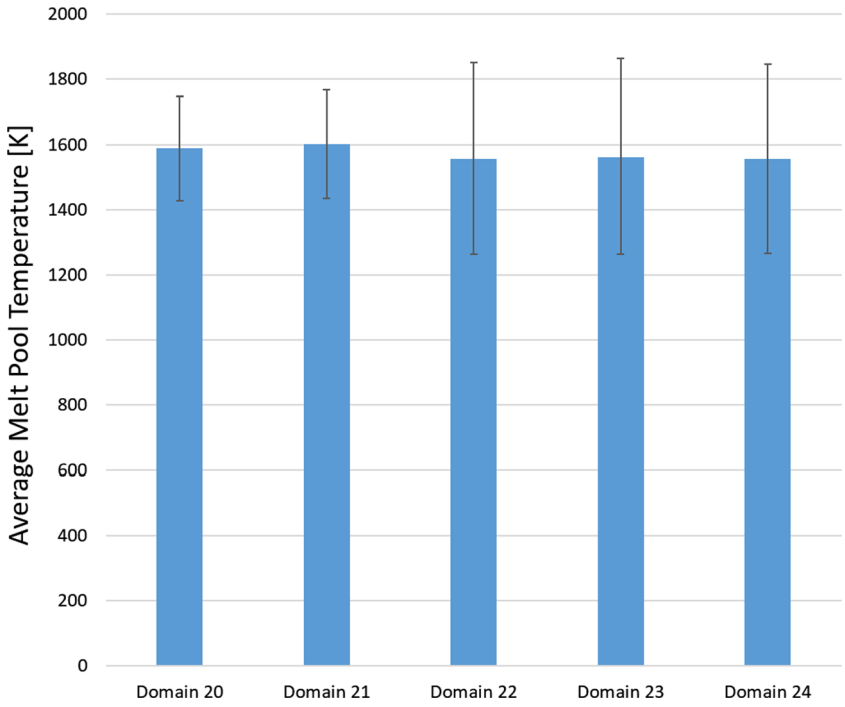

Fig. 19 Average melt pool temperature for studied powder beds

regime is identified (red region). In the opposite corner with low power and high scan speeds lack of fusion regime is identified (green region). In between these regions, an ideal window is shown in blue, where the porosity is lowest. The optimal process parameters identified above are shown by the white point. The chosen process parameters are comfortably in the center of the ideal process window, that small deviations of the build conditions during printing are not expected to affect material consolidation. The model validations, the calibration of the online monitors, and the central position of the chosen parameters in the process window enabled the locking of the process parameters for 718Plus®.

Distortion and Residual Stresses

The distortion and residual stress model described in [8] is used to analyze the manufacturability of the rocket nozzle and to predict the final shape of the body and different features to be assessed. The model was validated several times for powder bed fusion processes [25, 26]. Figure 23 shows the predicted as-built distortion after removal of the base plate from the printing chamber. The simulation was performed using the process parameters identified above. All downward facing surfaces indicate distortions in the order of 800 μm.

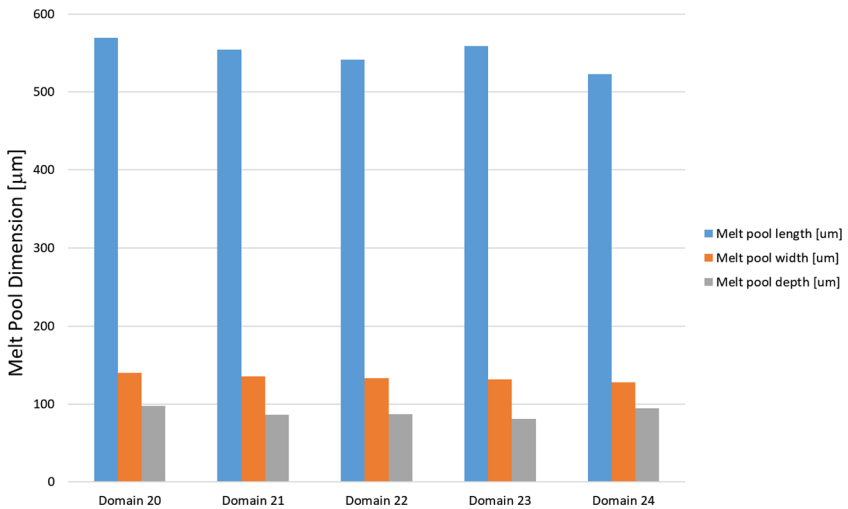

Fig. 20 Melt pool dimensions for studied powder beds

Table 3 Parameter values and bounds for UQ study of powder bed variations. The upper and lower bounds are engineering assumptions

Variable	Nominal value	Lower bound	Upper bound	Lower %	Upper %
Table displacement (μm)	30				
Laser power (W)	300	270	330	10%	10%
Spot size (μm)	80	76	84	5%	5%
Scan speed (m/s)	1.25	1.2375	1.2625	1%	1%

Numerical Manufacturability Assessment

The printing process might be interrupted if the re-coater arm interacts with the build leading to termination of the printing job. The vertical distortion predictions for each layer are analyzed in Fig. 24. Using the packing densities predicted by the spreading models [18], the gap between the build upper surface and the re-coater arm can be calculated and used as maximum permissible vertical distortion. Figure 24 shows that the rocket nozzle vertical distortion is safely below the gap size, that re-coater arm interaction is not expected.

Numerically Predicted Final Shape

Figure 25 shows as-built distortions of the rocket nozzle lower half. Computer tomography is used to check the quality of the internal thin walls. The numerically predicted thin wall thicknesses are within 4% of the CT measurements and correspond closely to the CAD definition. The thick wall deviates by up to 7% from the CAD dimension, as predicted using the distortion model.

Crack Risks

The integrity of the thin walls is checked to ensure that they will be printed without hot or cold cracking. Hot cracking is checked using the thermal gradients during solidification [31]. The model is complemented by constitutive laws for porous media [32, 33]. The crack susceptibility criterion was calculated for the process parameters chosen (power, scan speed, and hatch spacing) indicating no danger of hot cracking. Cold cracking on the other side is assessed by considering the as-built residual stress (Fig. 26, left) and plastic strains (Fig. 26, right). The stresses are not uniform and show localized peaks at the base of thin walls. The non-uniformity of the stresses is attributed to the changes in nozzle cross sections. Thicker sections, where ramps or flanges are foreseen, lead to higher residual stresses. The maximum stresses are at yield. The plastic strains correlate with the stress distributions observed. The maximum plastic strain is below 2%. 718Plus® has a maximum ductility of around 20%. It is thus concluded that cold cracking is not a major risk for this build.

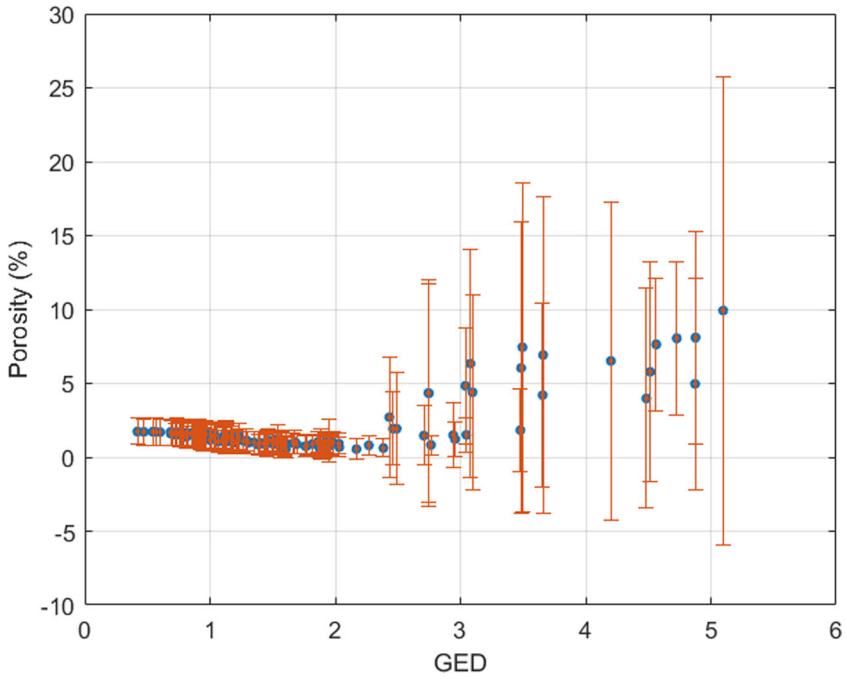

Fig. 21 Porosity as a function of global energy density. The standard deviations indicate porosity variation in processed material

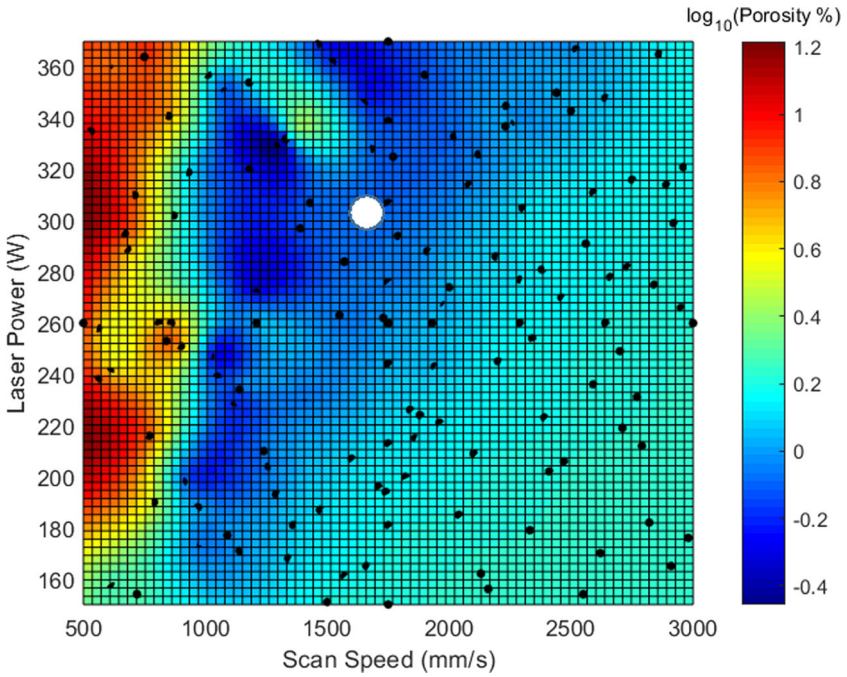

Fig. 22 Numerically compiled process map for 718Puls®. The white dot represents the previously identified optimal process parameters

First Build Assessment

The nozzle is only about 1-cm shorter than the capacity of the EOS M280. It is hence built in two different manners. In the first build, a single nozzle using a dosing factor of 2 was attempted. We found that the powder holder capacity is not enough to build such a tall part and we had to stop the build to add powder to complete the build. A witness mark remained in the nozzle because of this as shown in Fig. 27a. The second time, we built three nozzles positioned along the diagonal of the build plate and

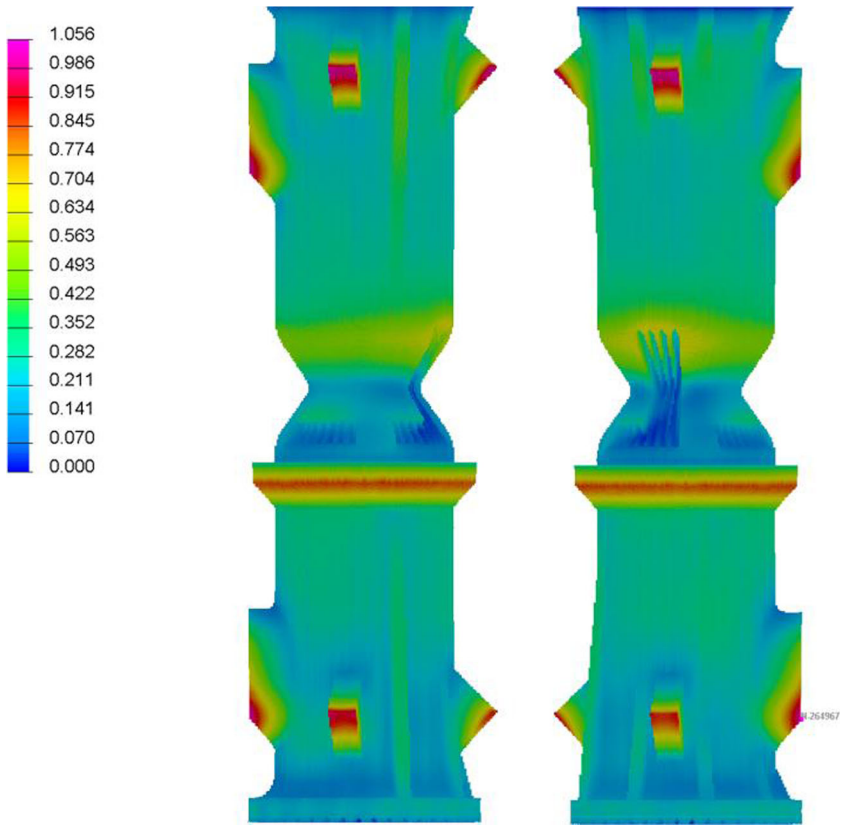

Fig. 23 As-built distortion after removal of the build plate from the printing chamber (mm)

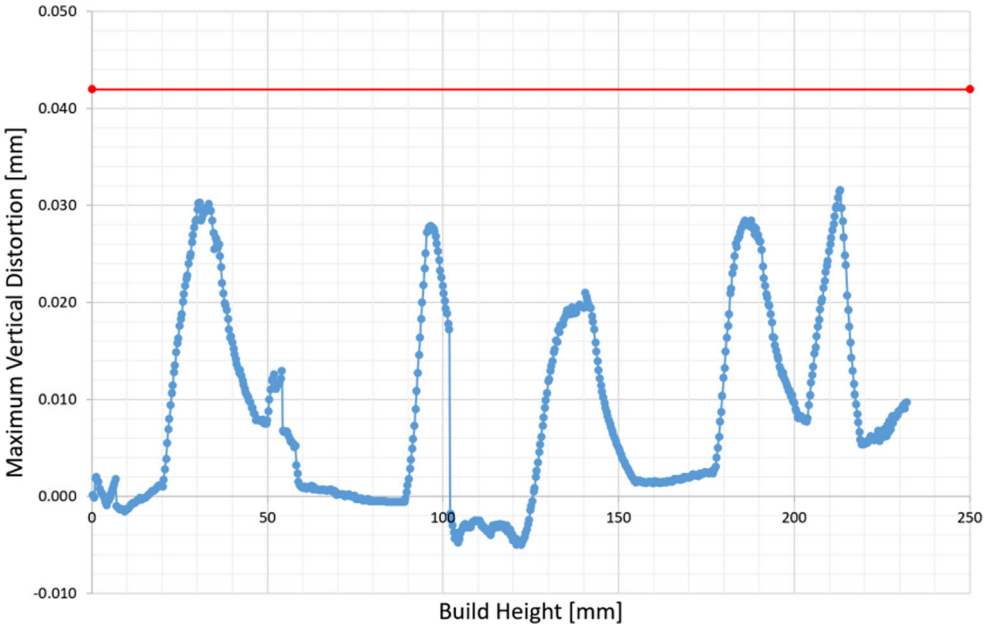

Fig. 24 Maximum vertical distortion for each layer during the build process

used a dosing factor of 1.5, the build completed successfully this time (Fig. 27b).

In-process Quality Signature

The In-Process Quality Metric (IPQM™) is a concept which uses a feature of the process to ascertain and then take action on the quality of the part built, it is used for quality control. One of those metrics is the TED™ Metric, it is computed by using the light emitted by the LPBF process and captured by a photodetector, the aggregate wide band wavelengths over a pixelated grid. The photodetector generates an electrical signal commensurate to the intensity of the light emitted and statistics are collected based on the variability of the intensity of the light for the build conditions of interest.

Data was collected for a group of builds of specimens at different processing conditions and a metric was developed and designated thermal emission density (TED™). The specimen porosity levels were measured and plotted against TED™ metric (Fig. 28). This figure also contains the measurements collected during the rocket nozzle build. The region highlighted by the yellow box was measured during the build

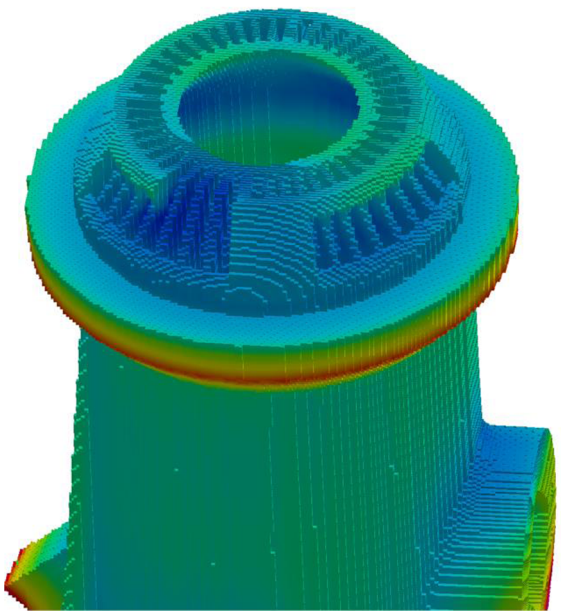

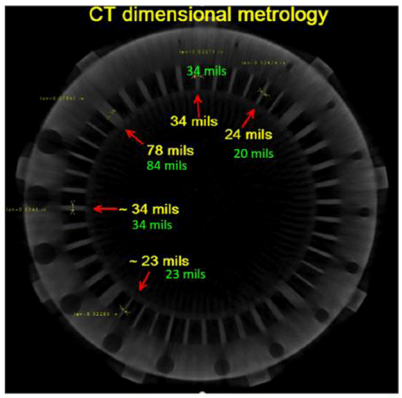

CAD [mils]	CT [mils]	ESI-AM [mils]
20	24	23
34	34	32
84	78	77
34	34	32
23	23	22

Fig. 25 Computer tomography of thin walls at the height shown in the 3D numerical prediction. The thickness as defined in the CAD model, as measured in CT images and as predicted by the model are compared in the table

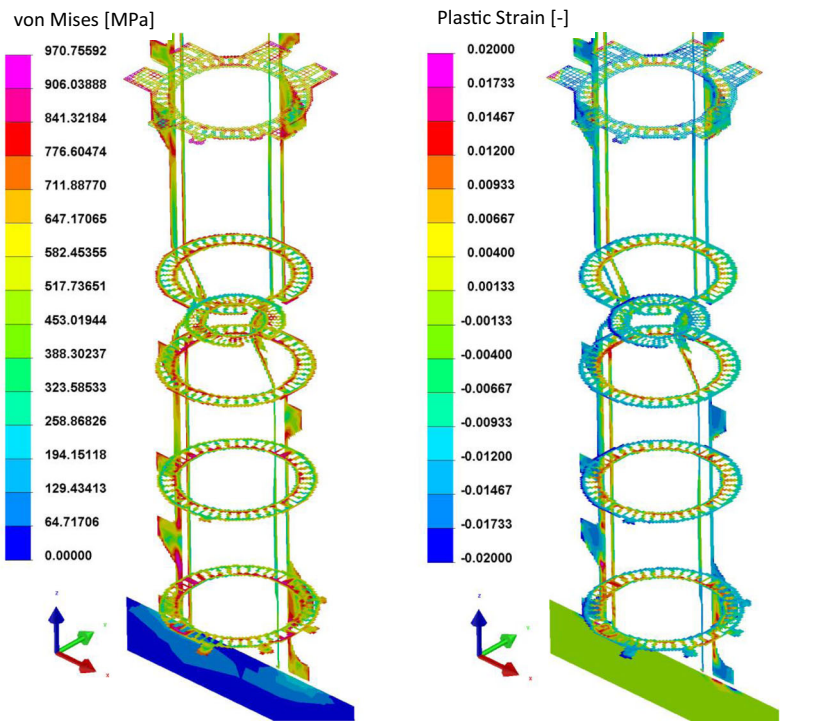

Fig. 26 Left: distribution of as-built von Mises residual stresses (MPa). Right: distribution of as-built plastic strain

and indicates that the porosity level would be between 0.2 and 0.4%. Metallurgical cross sections of one of the parts showed that the highest porosity was in the order of 0.1%, well within the shown scatter band of the data.

The left image on Fig. 28 was developed by building specimens at different build conditions each and their porosity measured afterwards, the red and blue circles correspond to two different sets of specimens built at different times. Measurements were also taken for specimens built with the optimum build conditions and the statistics of the process was calculated and limits developed using, for example, the WECO (Western Electric Company) rules [34]. The WECO rules are decision rules in statistical process control for detecting out of control or non-random conditions on control charts. Locations of the observations relative to the control chart control limits (typically at ± 3 standard deviations) and centerline indicate whether the process in question should be investigated for assignable causes.

The component of interest is then built with the optimum build conditions and the statistics of the component build are calculated and compared to the statistics of the specimen build at the optimum conditions. The component data is plotted in the control charts, as in Fig. 29, and a determination is made as to what actions to take; if in control no action, and if out of control to search for assignable causes.

TED™ metric is also used to create control charts to help analyze and review data with varying degrees of granularity. Figure 29 below shows an example chart for a group of specimens built for tensile testing. There was a total of seven builds. The average metric for the entire build for each specimen is calculated and plotted for each build and the process control limits defined using the first build. The figure shows that on each subsequent build the number of specimens falling off the control limits is increasing and thus maintenance for the machine was requested. Maintenance showed that the laser power output

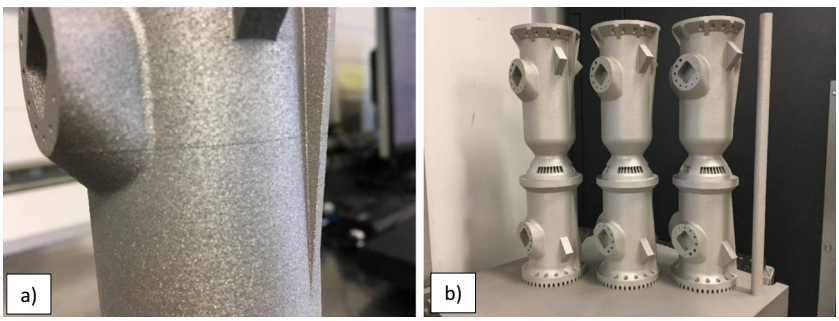

Fig. 27 **a** Witness mark due to stop to reload powder in order to complete the full run and **b** successful build of three nozzles using a dosing factor of 1.5

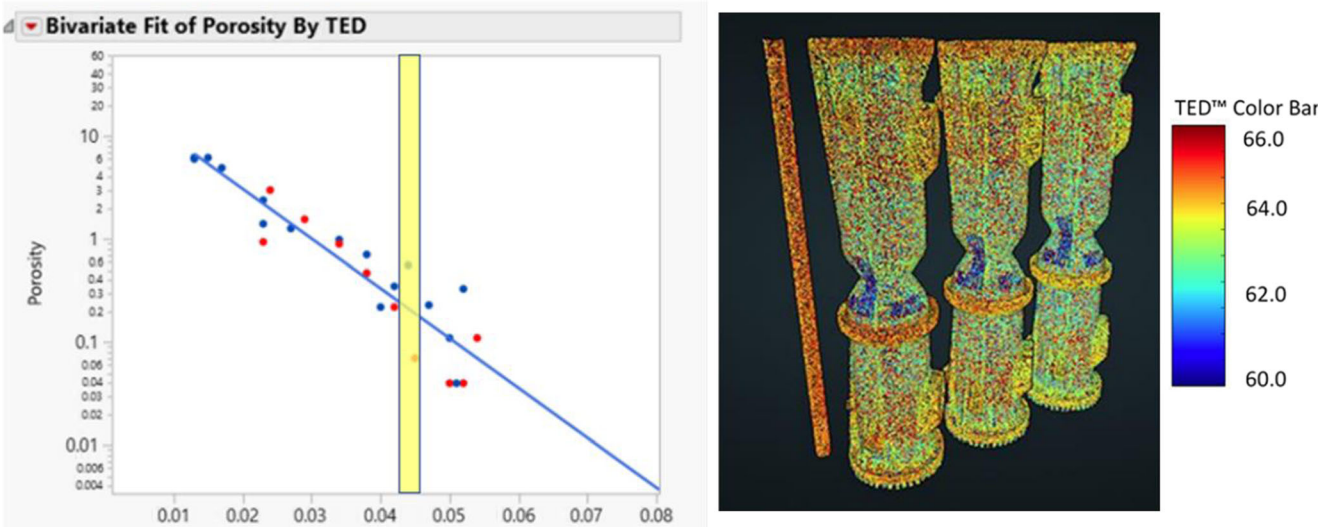

Fig. 28 Correlation of porosity and the quality metric (TED™) and measurement levels collected during the build (yellow band)

was out of specification and that it was outputting 50 W lower than commanded. The laser was changed and the metric for the last set of specimens is shown to be out of control on the upper limit. The conclusion is that the laser was already faulty at the time when the first set of specimens was built.

Rocket Nozzle Porosity

The nozzle was sectioned for metallographic evaluation to determine the porosity of the build. Measurements show, Fig. 30, that the porosity of the sample is less than 0.1%. It is also important to highlight that the porosity of the thin sections is relatively higher than those of the thick section.

NDT of Nozzle—CT Scan

The rocket nozzle was processed through a CT scan to test the resolving power and sensitivity of CT (detection of side drilled holes (SDH) on various surfaces and orientations, various fin thicknesses, etc.). Due to large differences in the thickness, there were areas of significant signal loss. X-ray energy high enough to penetrate these areas saturated the detector in the regions where the cross section was the thinnest, so a "compromised" energy was selected that would be suitable to image the nozzle in its entirety. Areas highlighting the resulting regions of poor contrast are shown in Fig. 31. Fin dimensions as well at the SDH from the bottom are shown in Fig. 32. CT could identify 356 μm SDH and verified the thickness of a 610 μm fin.

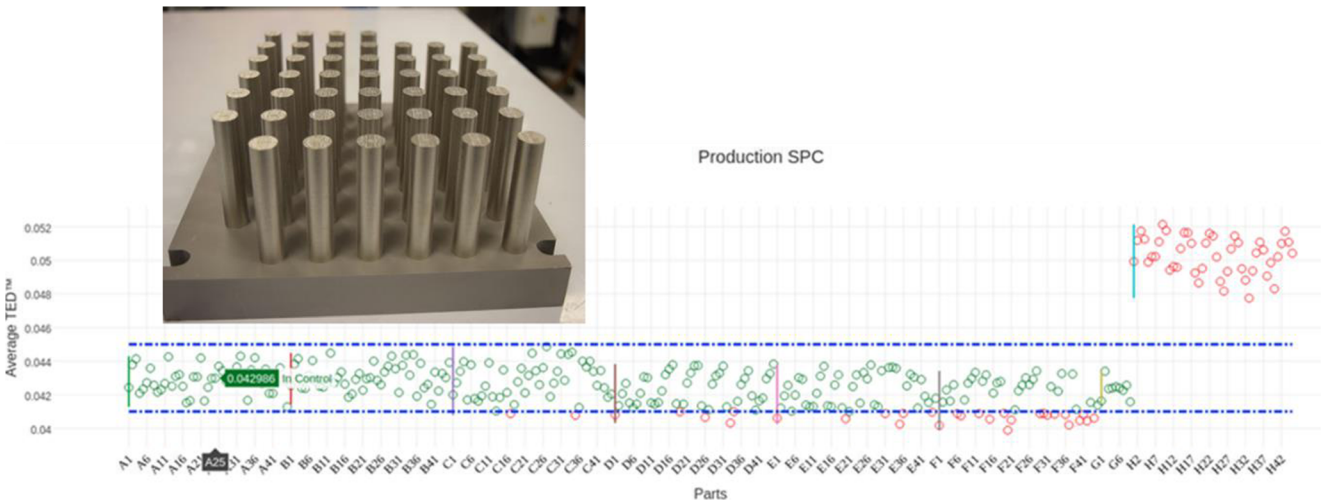

Fig. 29 Statistical process control for the specimen build in the specimens shown. The TED™ metric can be used to monitor the AM equipment health

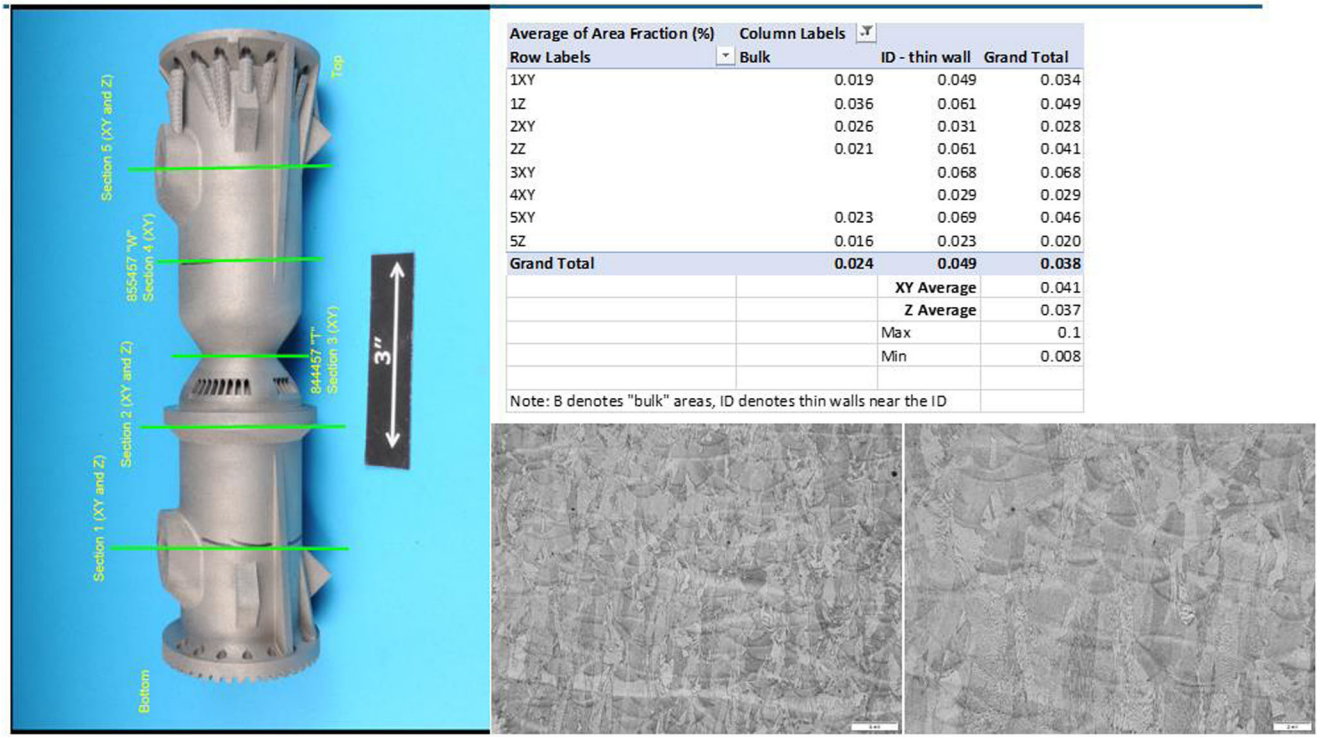

Average of Area Fraction (%)	Column Labels		
Row Labels	Bulk	ID - thin wall	Grand Total
1XY	0.019	0.049	0.034
1Z	0.036	0.061	0.049
2XY	0.026	0.031	0.028
2Z	0.021	0.061	0.041
3XY		0.068	0.068
4XY		0.029	0.029
5XY	0.023	0.069	0.046
5Z	0.016	0.023	0.020
Grand Total	**0.024**	**0.049**	**0.038**
		XY Average	0.041
		Z Average	0.037
		Max	0.1
		Min	0.008
Note: B denotes "bulk" areas, ID denotes thin walls near the ID			

Fig. 30 Measurements of porosity levels using metallographic cross-sections of the article

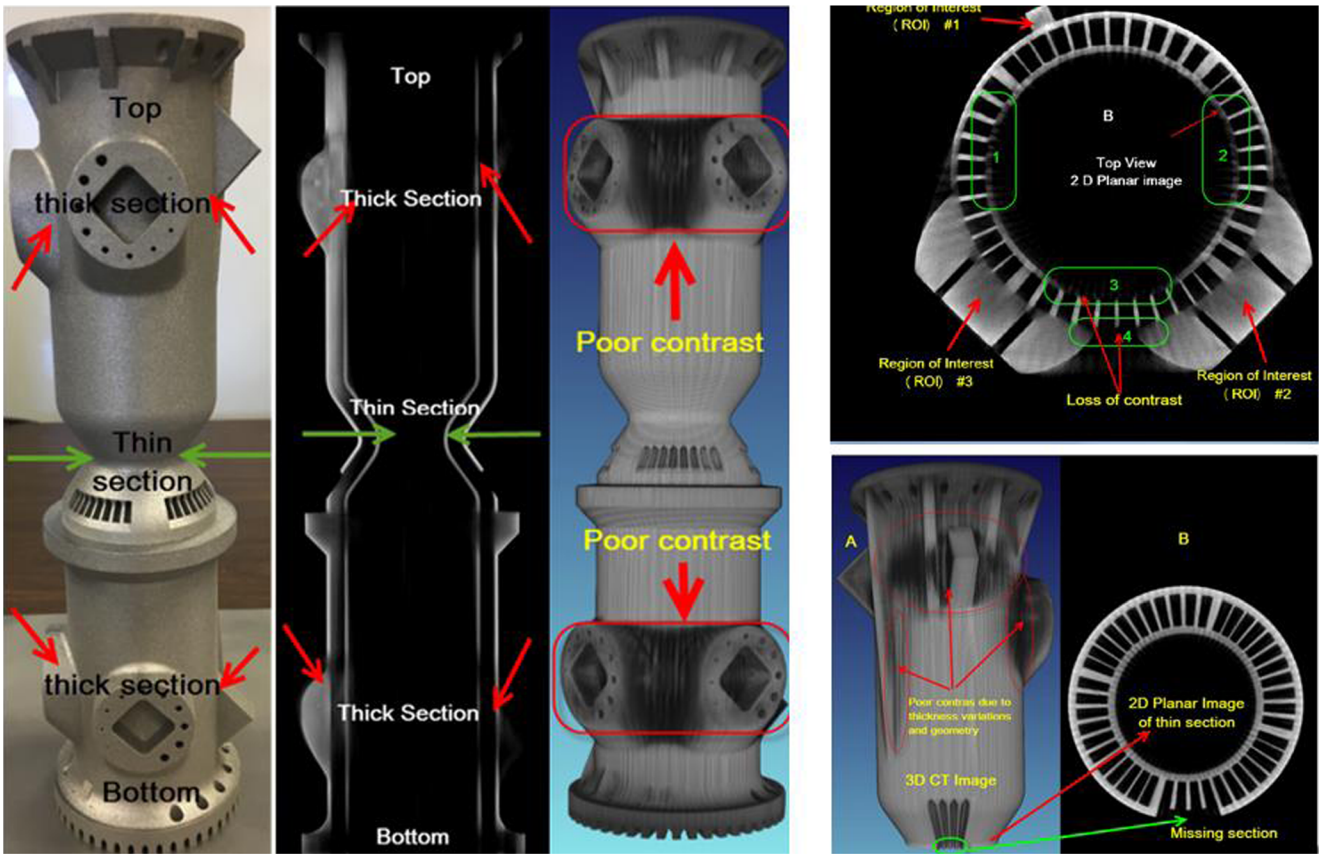

Fig. 31 CT measurements of the article of interest

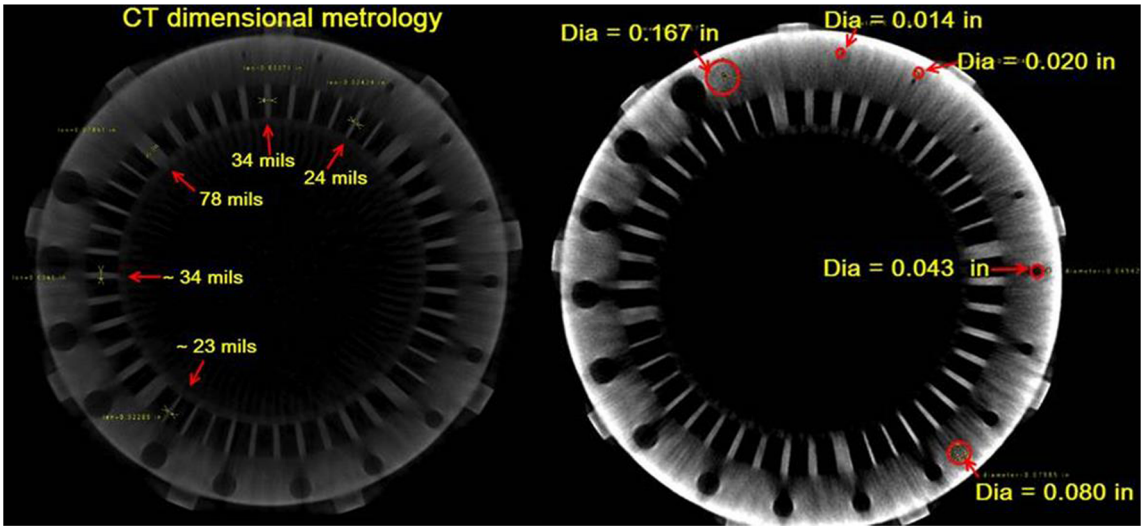

Fig. 32 Fin dimensions to assess dimensional fidelity of the build

Nozzle Burst Test

The nozzles were cut into three sections in order to test their strength by applying an internal pressure. The nozzle throat section was cut and discarded, and the remaining two cylindrical sections were prepared and installed in a fixture that capped both ends and a pressure was applied internally. The nozzles failed at an ultimate internal pressure that ranged from 16,800 to 20,600 Psi at the location shown in Fig. 33. The applied pressure vs. measured strain is shown in Fig. 34 for one of the articles. The yield strength of the material, calculated using the strain-pressure curve, corresponds to 150 ksi.

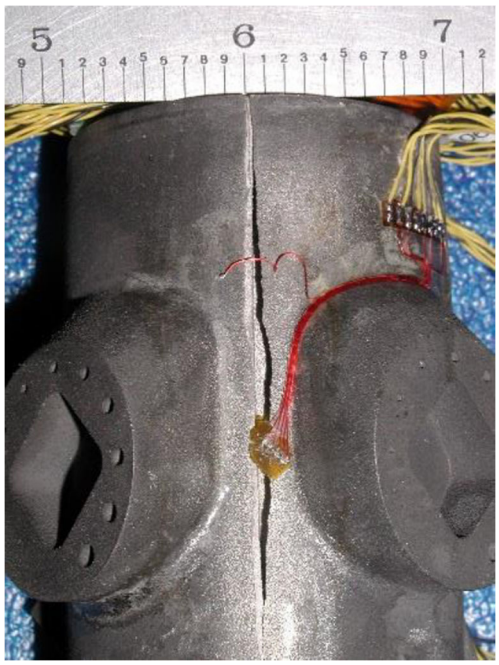

Fig. 33 Failure location of the nozzle due to internal pressure in the inner diameter of the article

The strength of the alloy has been shown through specimen testing to be on average 138 ksi. Interestingly, the component yield strength is higher than the yield strength of the specimens. One possible reason for this difference could be the article thickness which could lead to changes in the microstructure leading to a higher strength.

Summary and Conclusions

Qualification and/or certification is a process through which compliance to a set of requirements is demonstrated. The purpose of the qualification framework presented is to show that compliance can be demonstrated via numerical simulations supported by experiments for validation and calibration. The reason this approach is necessary is lack of experience and design rules for LPBF process. The qualification platform was developed to facilitate gaining insight into how the manufacturing process works and hence avoid pitfalls. The software capabilities to analyze the melting of the powder was used to ensure that the selected process conditions (speed, power, hatch spacing, and layer thickness) yields very low levels of porosity in the as-build condition. The distortion capabilities were used to confirm that the component meets dimensional requirements and furthermore that the build process will not experience any stoppages due to re-coater collisions with the workpiece. Simulations were also used to evaluate potential hot and cold crack susceptibility of the material and the component via thermal gradients of the melt pool and the residual stress and strains, respectively.

Experiments are presented which help ascertain the accuracy of the numerical predictions. The porosity predictions were compared to those of specimens built at different conditions. The porosity was measured via metallographic cross sections as well as Archimedes method. The same trends and values were

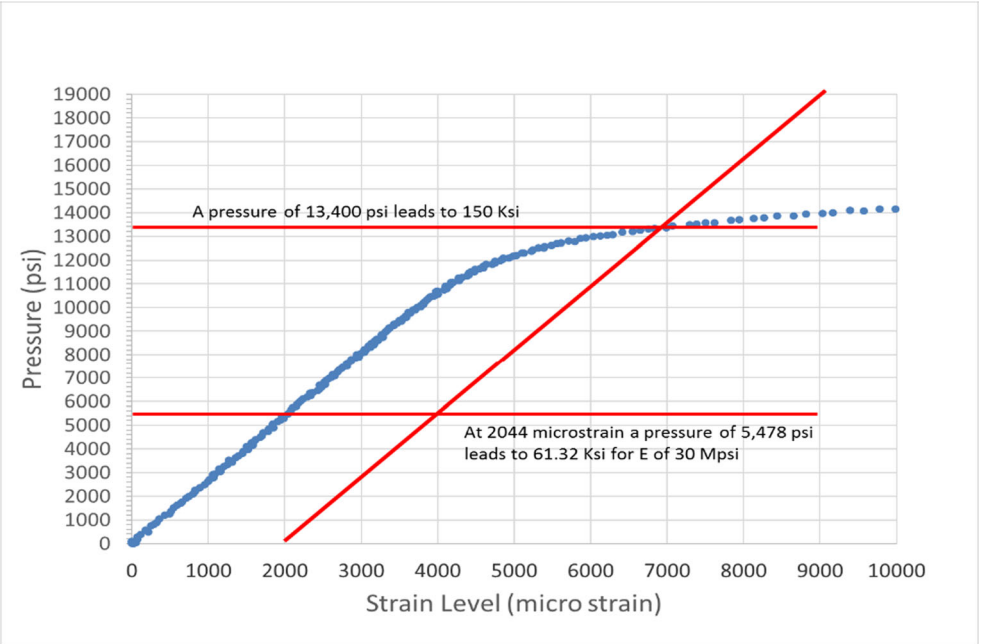

Fig. 34 Internal pressure vs. measured strain behavior of the nozzle. Corresponding yield strength is computed using the product of the strain and the modulus of elasticity, as shown in the image a yield strength of 150 ksi is obtained

observed as those predicted. The melt pool temperature and melt pool size were compared to images gathered via a two-wavelength digital camera. The melt pool temperature comparison is within a 100 K at temperatures at the boiling point of the metal (~3000 K). The melt pool size, width and length, was more difficult to compare and further work is needed to understand the comparisons.

Sensors were used to develop an IPQM™ that can be used to monitor the quality of the component, with respect to porosity, as it is being built. A photodetector was used to collect light emitted by the process and the electrical response analyzed and its statistics computed and used to develop process control limits. Specimens were built at optimum and off optimum process conditions and process data collected and plotted against the quality metric (TED™), the response of the rocket nozzle was plotted against those of the specimens and showed that the level of porosity of the component is well within the acceptable range and which was also verified experimentally.

This work has demonstrated that a combination of physics based modeling and experimental verification and validation can enable early stage identification and elimination of potential problems. The build was directly successful and component testing confirmed achievement of the targeted porosity, geometric accuracy, and mechanical strength of the printed material. It has shown that the qualification framework presented here can be used as the compliance means for certifications and/or certification of components.

Authors' Contributions All authors contributed to the effort described in this article.

Funding Information This study is financially supported by the DARPA Open Manufacturing program, USA.

Compliance with Ethical Standards

Competing Interests The results presented in this work are that of the team involved in the DARPA Open Manufacturing program. References to literature and results of other research teams are made neutrally to gain better understanding of the modeling algorithms and the implications for real-life applications.

References

1. Frazier WE (2014) Metal additive manufacturing: a review. JMEPEG. 23:1917–1928. https://doi.org/10.1007/s11665-014-0958-z
2. Seifi M, Salem A, Beuth J, Harrysson O, Lewandowski JJ (2016) Overview of materials qualification needs for metal additive manufacturing. JOM. 68(3):747–764. https://doi.org/10.1007/s11837-015-1810-0
3. (2014) Additive manufacturing strategic research agenda 2014. AM Platform, https://www.rm-platform.com/linkdoc/AM%20SRA%20-%20February%202014.pdf
4. Peralta AD, Enright M, Megahed M, Gong J, Roybal M, Craig J (2016) Towards rapid qualification of powder bed laser additively manufactured parts. Integr Mater Manuf Innov 5:8. https://doi.org/10.1186/s40192-016-0052-5
5. C. Kamath B. Eldasher, GF Gallegos, WE King A Sisto (2013) Density of additively-manufactured, 316L SS parts using laser powder-bed fusion at powers up to 400 W. LLNL-TR-648000 Lawrence Livermore National Laboratory
6. Tang M, Pistorius PC, Beuth JL (2017) Prediction of lack-of-fusion porosity for powder bed fusion. Addit Manuf 14:39–48. https://doi.org/10.1016/j.addma.2016.12.001
7. Hann DB, Iammi J, Folkes J (2011) A simple methodology for predicting laser-weld properties from material and laser parameters.

J Phys D Appl Phys 44. https://doi.org/10.1088/0022-3727/44/44/445401
8. Megahed M, Mindt HW, N'Dri N, Duan HZ, Desmaison O (2016) Metal additive manufacturing process and residual stress modelling. Integr Mater Manuf Innov 5. https://doi.org/10.1186/s40192-016-0047-2
9. Attar E (2011) Simulation der selektiven Elektronenstrahl schmelzprozesse. PhD Thesis University of Erlangen-Nuremberg
10. Körner C, Attar E, Heinl P (2011) Mesoscopic simulation of selective beam melting processes. J Mater Process Technol 211:978–987. https://doi.org/10.1016/j.matprotec.2010.12.016
11. Körner C, Bauereiß A, Attar E (2013) Fundamental consolidation mechanisms during selective beam melting of powders. Model Simul Mater Sci Eng 21(085011):18pp. https://doi.org/10.1088/0965-0393/21/8/85011
12. Klassen A, Scharowsky T, Körner C (2014) Evaporation model for beam based additive manufacturing using free surface lattice Boltzmann methods. J Phys D Appl Phys 47(275303):12. https://doi.org/10.1088/0022-3727/47/27/275303
13. King WE, Barth HD, Castillo VM, Gallegos GF, Gibbs JW, Hahn DE et al (2014) Observation of keyhole-mode laser melting in laser powder-bed fusion additive manufacturing. J Mater Process Technol 214:2915–2925. https://doi.org/10.1016/j.jmatprotec.2014.06.005
14. King WE, Anderson AT, Ferencz RM, Hodge NE, Kamath C, Khairallah SA et al (2015) Laser powder bed fusion additive manufacturing of metals; physics, computational, and materials challenges. Appl Phys Rev 2:041304. https://doi.org/10.1063/1.4937809
15. Kovaleva I, Kovalev O, Smurov I (2014) Model of heat and mass transfer in random packing layer of powder particles in selective laser melting. Phys Procedia 56:400–410. https://doi.org/10.1016/j.phpro.2014.08.143
16. Mindt HW, Megahed M, Peralta A, Neumann J (2015) DMLM models - numerical assessment of porosity. 22nd ISABE Conference, Oct. 25–30, Phoenix, AZ., USA
17. Mindt HW, Megahed M, Shula B, Peralta AD, Neumann J (2016) Powder bed models - numerical assessment of as-built quality. AIAA ,SciTech, 4-8 January, San Diego. https://doi.org/10.2514/6.2016-1657
18. Mindt HW, Megahed M, Lavery NP, Holmes MA, Brown SGR (2016) Powder bed layer charateristics: the overseen first-order process input. Metall Mater Trans A 47(8). https://doi.org/10.1007/s11661-016-3470-2
19. Feulvarch F, Robin V, Bergheau JM (2011) Thermometallurgical and mechanical modelling of welding - application to multipass dissimilar metal girth welds. Sci Technol Weld Join 16(3):221–226
20. Michaleris P (2014) Modeling metal deposition in heat transfer analyses of additive manufacturing processes. Finite Elem Anal Des 86:51–60
21. Denlinger ER, Heigel JC, Michaleris P (2014) Residual stress and distortion modeling of electron beam direct manufacturing Ti-6Al-4V. J Eng Manuf 1:1–11
22. Heigel JC, Michaleris P, Reutzel EW (2015) Thermo-mechanical model development and validation of directed energy deposition additive manufacturing of Ti-6Al-4V. Addit Manuf 5:9–19
23. Keller N, Ploshikhin V (2014) Fast numerical predictions of residual stress and distortion of AM parts. 1st International Symposium on Material Science and Technology of Additive Manufacturing, Bremen, Germany
24. Neugebauer F, Keller N, Ploshikhin V, Feuerhahn F, Köhler H (2014) Multi scale FEM simulation for distortion calculation in additive manufacturing of hardening stainless steel. International workshop on thermal forming an welding distortion, Bremen, Germany
25. Desmaison O, Pires PA, Levesque G, Peralta A, Sundarraj S, Makinde A, et al. (May 21–25, 2017) Influence of computational grid and deposit volume on residual stress and distortion prediction accuracy for additive manufacturing modeling. 4th World congress on integrated computational materials engineering - ICME 2017, Ypsilanti, Mi, USA
26. Pires PA, Desmaison O, Megahed M (2018) ICME manufacturability assessment in powder bed fusion additive manufacturing. JOM. 70(9):1677–1685. https://doi.org/10.1007/s11837-018-3024-8
27. Mindt HW, Desmaison O, Megahed M, Peralta A, Neumann J (2018) Modelling of powder bed manufacturing defects. J Mater Eng Perform 27(1):32–43. https://doi.org/10.1007/s11665-017-2874-5
28. (2011) ATI 718 Plus alloy data sourcebook. : Revision 1.2, ATI Allvac
29. Chinestra F, Leygue A, Bordeu F, Aguado JV, Cueto E, Gonzalez D et al (2013) PGD-based computational vademecum for efficient design, optimization and control. Arch Comput Methods Eng 20:31–59. https://doi.org/10.1007/s11831-013-9080-x
30. Chinesta F, Keunings R, Leygue A. (2014) The proper generalized decomposition for advanced numerical simulations. A primer. Cham Heidelberg New York Dordrecht London: Springer
31. Bertoli US, Wolfer A, Matthwes MJ, Delplanque J-PR, Schoenung JM (2017) On the limitations of volumetric energy density as a design parameter for selective laser melting. Mater Des 113:331–340. https://doi.org/10.1016/j.matdes.2016.10.037
32. Rappaz M, Drezet JM, Gremaud M (1999) A new hot tearing criterion. Met Trans 30A:449–455
33. Boying TB, Grathwohl P (2001) Tracer diffusion coefficients in sedimentary rocks: correlations to porosity and hydraulic conductivity. J Contam Hydrol 53(1–2):85–100
34. Western Electric Company (1956) Statistical quality control handbook, 1st edn. Western Electric Co., Indianapolis

Publisher's Note Springer Nature remains neutral with regard to jurisdictional claims in published maps and institutional affiliations.